

Multi-stage 3D Gravity Inversion Scheme for Maximum Optimization of the Subsurface Basement Model at Gebel El-Zeit Basin, Southwestern Gulf-of-Suez, Egypt

Ahmed Gamal Mohamed HASSAN^{1,2*}

Karam Samir Ibrahim FARAG³

Alaa Ahmed Fahmi AREF²

Alexey Lazarevich PISKAREV¹

¹Saint Petersburg State University, Saint Petersburg, Russia

²Nuclear Materials Authority (NMA), Cairo, Egypt

³Ain shams University, Cairo, Egypt

Abstract

Relevance and purpose of the work. Due to its basement fault block pattern in the sedimentary basin, the Southwestern Gulf of Suez's Gebel El-Zeit basin is one of Egypt's most desirable hydrocarbon concessions. However, salt diapers in sedimentary layers have hindered seismic interpretations in this area, making it challenging to build a 3D central primary basinal structure. This study uses Bouguer gravity anomalies to input basement complex lateral density model assumptions to determine the optimal three-dimensional basement depth for the study area.

Research methodology. Based on the concept of sequential 3D spectral layered-earth inversion approaches, through trials with the Oldenburg and other forward models, many forward optimization strategies and parameterization sequences with variable constraint parameter assumptions were used to regulate the inversion operations within a proposed three-stage gravity inversion scheme to identify the optimal depth-density solution with a minimal computational data misfit. This study statistically analyzes the basement's relief and complicated lateral density distribution to determine the best parameters for a 3D depth-density model solution. Zero regional gravity offset and DC-shift, which forced the mean error to be zero, helped simulate the lateral density model's best-possible constraining assumptions.

Results and conclusions. Correlating depth data from many stratigraphical-control wells drilled in the inverted 3D basement model confirmed the basement relief optimality of the study area. Correlation analysis showed a good match between the predicted and measured depths, proving the resulting optimality of the basement complex's lateral density distribution, minimizing the computational depth error to a minimal percentage.

Keywords: Egypt, Gulf of Suez, El Zeit Basin Area, Bouguer anomalies, spectral layered gravity inversion scheme, parameterizations and optimization.

Introduction

Gravitational anomalies inversely help in recovering sedimentary basins, tectonics, and petroleum-rich places. Given the source's depth, thickness, and shape, determining the basement's undulating surface morphology from gravity measurements is a nonlinear inverse problem. Different source assumptions may create discrepancies when determining sedimentary basin basement depth. The forward Fast Fourier Transform (FFT) method estimates undulating layer gravitational or magnetic influences [1, 2].

The slab formula ($g = 2\pi\gamma\Delta\rho t$) predicts sediment thickness at each gravity datum utilizing just the gravitational constant (g), density contrast ($\Delta\rho$), and slab thickness (t). Iterative modeling shows nonlinearity [3]. Later articles modified the technique by increasing iterations, converting to a density-depth function instead of a constant density, and re-evaluating the fitting function.

The Bott's iterative procedure's step sizes was adjusted based on the model's ratio of observed to estimated gravity

anomalies [4]. Silva suggested testing the model if the L_2 norm of the residual vector is lower than in the previous iteration to speed convergence [3]. The density matched the gravity model (drill hole gravity data, gamma-gamma density, and saturated or unsaturated sample density measurements). Linear, quadratic, exponential, hyperbolic, and parabolic models reveal that density growth is most significant towards the surface [5–8]. The environment affects sediment density.

Density data may not match the density contrast function from density measurements at a few basin locations, making depth-dependent density contrast challenging to establish [8]. Gravity modeling in sedimentary basins may benefit from non-density contrast interpretation methods.

Backward computing on the model's iteration field yields the analytic solution for the gravity field of a two-dimensional polygonal body, a three-dimensional rectangular prism, or a complex undulating layer [3]. Fourier-domain operations are faster than space-domain operations, as Bott's technique

*ahmed.gamal_88@hotmail.com

avoids matrix multiplications and inversions. Formulas for polyhedral bodies with a linear density contrast function, analytical formulas for prismatic bodies with a parabolic [9] or cubic polynomial [10] function, and algorithms for modeling the vertical variation of density contrast with depth all require an exponential or cubic polynomial fitting function [6, 11, 12]. Jachens calculated the basement's growing density's gravitational impact and created measures to minimize it using Bott's approach [13]. Phelps examined Nevada's Yucca Flat basin isostatic anomalies [8].

Tikhonov's regularized inversion estimates basement geometry for interpreting gravity data [14]. Inverting subsurface columns into prisms with known horizontal dimensions and densities predicts column thicknesses. The L_2 norm of the discrete first-order derivative of the model's objective function helps regularize the solution. Martins used

the L_1 norm of the discrete derivative total variation function to avoid penalizing quick morphological changes during basement depth inversion [15]. Sun employed nonlinear inversion to restore smoothness and blockiness to the model [16]. Two early inversions split the research area into smooth-and blocky-density contrast zones. The last inversion reduces the L_p model norm.

Feng established a nonlinear inverse approach that minimizes an objective function by adjusting model smoothness in the target area using a composite regularizing function [17]. Edge analysis or first-approximation models identify unique gravity anomalies. Nonlinear modeling estimates basement morphology and constant density contrast [18]. Li and Portniaguine modeled sedimentary basins without basement estimators [19, 20]. Regularized inversion is problematic because objective function stabilizers impact

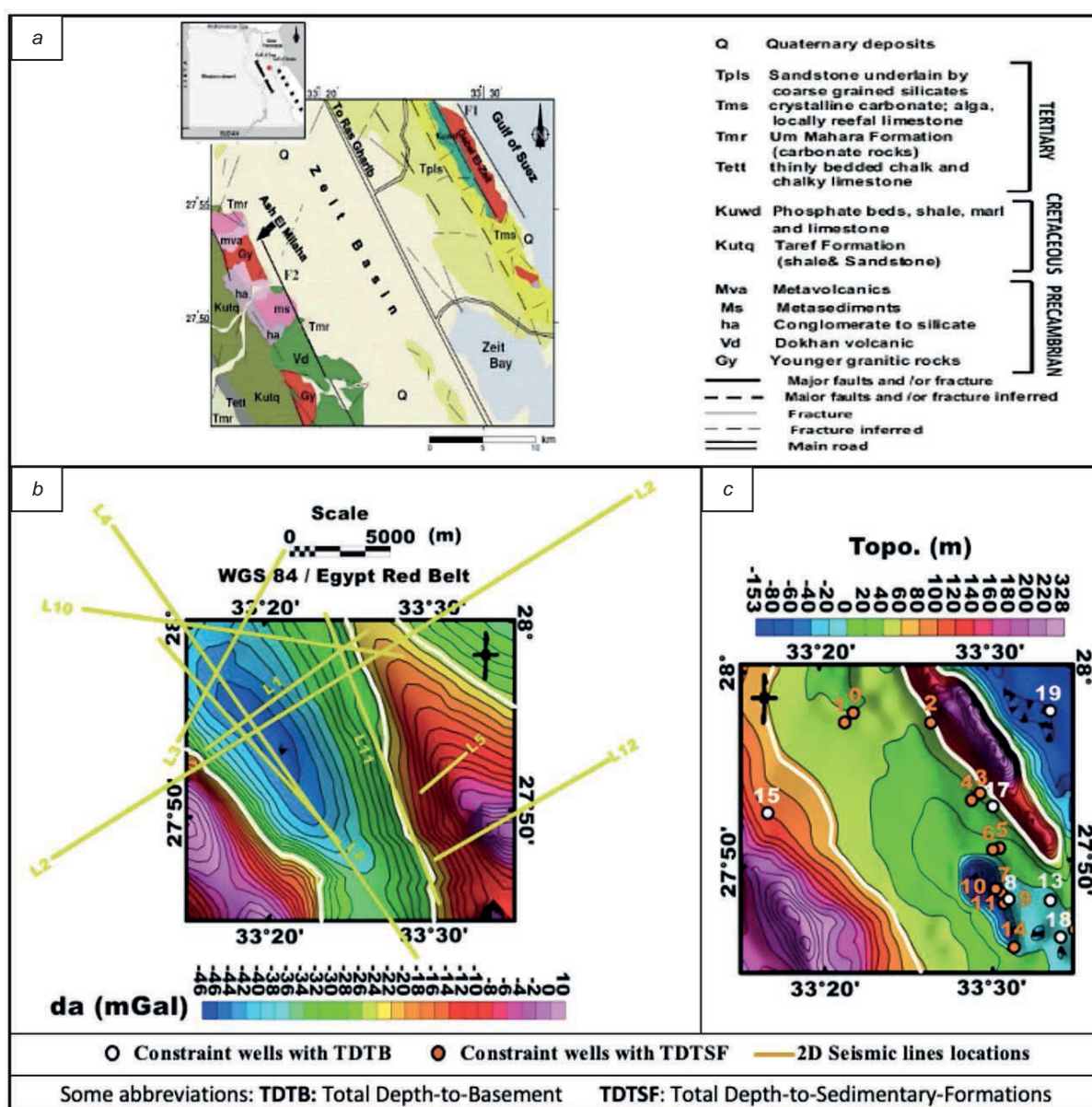


Figure 1.1. Data and geological setting: a – surface geologic map “after [34]”; b – Bouguer gravity anomaly contour map; c – Topographic contour map

Рисунок 1.1. Данные и геологическая обстановка: а – геологическая карта поверхности «по [34]»; б – контурная карта гравитационной аномалии Буге; в – топографическая контурная карта

Table 1. The reachable and unreachable basement constraint wells that we used to constrain and evaluate the optimality of the inverse depth model results of our inversion scheme in the study area [35, 36]

Таблица 1. Достижимые и недостичимые скважины, ограничивающие фундамент, использованные для ограничения и оценки оптимальности результатов модели инверсивной глубины нашей схемы инверсии на исследуемой территории [35, 36]

Well symbol	Well Name	Total Drilled Depth, m	Company	Status
<i>1st group / wells with T.D Reached Rock Unit [Basement] @ geologic age/ Pre-Cambrian</i>				
W8	C9A-1	2577	Conoco	Abandoned tested oil and gas
W13	QQ89-11	1129	DEOCO	Abandoned
W15	Wadi Dib #1	3769	CHEV EGY	Abandoned
W17	Gazwarina # 1	2162	Marathon	Suspended oil
W18	QQ89-3	2908	SUCO	Abandoned
W19	ERDMA-2	4051	Published [37]	
<i>2nd group / wells with T.D Reached Rock Unit [Nubia Sandstone (Nu)] @ geologic age / Carboniferous-Jurassic</i>				
W2	Kabrite west-1	1272	Petrozeit	Abandoned oil stain
W3	Gazwarina-2	1272	Marathon	Abandoned oil shows
W5	Gebel El Zeit-west-1	1966	Deminex	Abandoned
W6	Gebel El Zeit-west-2	2195	Deminex	Abandoned
W11	East Ras Gemsa-4	2542	Gupco	Abandoned gas shows
<i>3rd group / wells with T. D Reached Rock Unit [Matulla Formation (Ma)] @ geologic age / Upper Cretaceous</i>				
W9	Khalig El Zeit-1	2509	Devon	Abandoned
W10	East Ras Gemsa-2	2538	Gupco	Abandoned
W16	Zeit Bay 1	4452	CHEV EGY	Abandoned
<i>4th group / wells with T.D Reached Rock Unit [Nukhul Formation(Nuk)] @ geologic age / Lower Miocene</i>				
W0	Gebel El Zeit-2	3743	GPC	Abandoned
<i>5th group / wells with T.D Reached Rock Unit [Rudies Formation (Ru)] @ geologic age / Lower Miocene</i>				
W1	Ramadan-1	3760	GPC	Abandoned oil and gas shows
W4	Gazwarina-3	951	Marathon	Abandoned
W7	C9A-3	2122	Conoco	Abandoned
W14	C9B-1	3183	Conoco	Abandoned

Table 2.1. An explanation of any acronyms that may be used, along with a taxonomy of the different parameters used in our inversion scheme's parameterization of the forward and inverse models

Таблица 2.1. Объяснение любых сокращений, которые могут использоваться, а также таксономия различных параметров, используемых в параметризации нашей схемы инверсии прямой и инверсной моделей

Type	Parameter	Parameterization meaning
Root-mean-square and coefficient of variance evaluation parameters	$RMSD_{DTBo}$	Root-mean-square deviation of the initial-hypothesized depth-to-basement
	$RMSD_{DTBe}$	Root-mean-square deviation of the inversely estimated recovered depth-to-basement
	$CV - RMSD_{DTBo}$	The initially hypothesized depth-to-basement's root-mean-square deviation coefficient of variation
	$CV - RMSD_{DTBe}$	The inversely estimated recovered depth-to-basement's root-mean-square deviation coefficient of variation
	$CV - RMSD_{rb0}$	The initially hypothesized homogenous basement complex's density's root-mean-square deviation coefficient of variation
	$CV - RMSD_{rbe}$	The inversely estimated-recovered homogenous basement complex's density's root-mean-square deviation coefficient of variation
	$CV - RMSD_{LDDbo}$	The initially hypothesized basement complex's lateral density distribution's root-mean-square deviation coefficient of variation
	$CV - RMSD_{LDDbe}$	The inversely estimated recovered basement complex's lateral density distribution's root-mean-square deviation coefficient of variation
Depth and density model key parameters	$DTBa$	Depth-to-basement actually measured
	DTB_0	Depth-to-basement initially hypothesized
	$DTBe$	Depth-to-basement inversely estimated
	ρb_0	Basement complex's initial hypothesized homogenous density
	ρbe	Basement complex's inverse estimated recovered homogenous density
	$LDDb_0$	Basement complex's initial hypothesized lateral density distribution
	$LDDbe$	Basement complex's inverse estimated recovered lateral density distribution

solution fundamental features, regularization parameters, and model parameter restrictions.

Several basement depth measurements geologically confine ITRESC approaches, which approximate density

depth or contrast function. ITRESC will be tested in Egypt's southwest Gulf of Suez El Zeit basin with results comparison.

A prior information and geological setting. The Gulf of Suez formed when the African and Arabian tectonic plates

Table 2.2. (continued)
Таблица 2.2. (продолжение)

Density contrast model key parameters	$\Delta\rho(b-s)_0$	Sedimentary-Basement's initially-hypothesized homogenous density contrast interface
	$\Delta\rho(b-s)e$	Sedimentary-Basement's inversely-estimated recovered homogenous density contrast interface
	$\Delta\rho(LDDb-s)_0$	Sedimentary-Basement's initially-hypothesized lateral density contrast interface distribution
	$\Delta\rho(LDDb-s)e$	Sedimentary-Basement's inversely-estimated recovered lateral density contrast interface distribution
Inversion process constraint parameters	DC shift	DC shift
	Reg. offset	Regional offset
	Cnv. limit	Convergence limit
	Flt. LHC limit	Lower high cut limit Filter
	Flt. UHC limit	Upper high cut limit Filter
Data and data misfit parameters	da	Bouguer anomalies actual-observed data
	d_0	Bouguer anomalies initially-hypothesized
	de	Bouguer anomalies inversely-estimated
	Δde	Residual bouguer anomalies as an indicator for inversely-estimated recovered data misfit

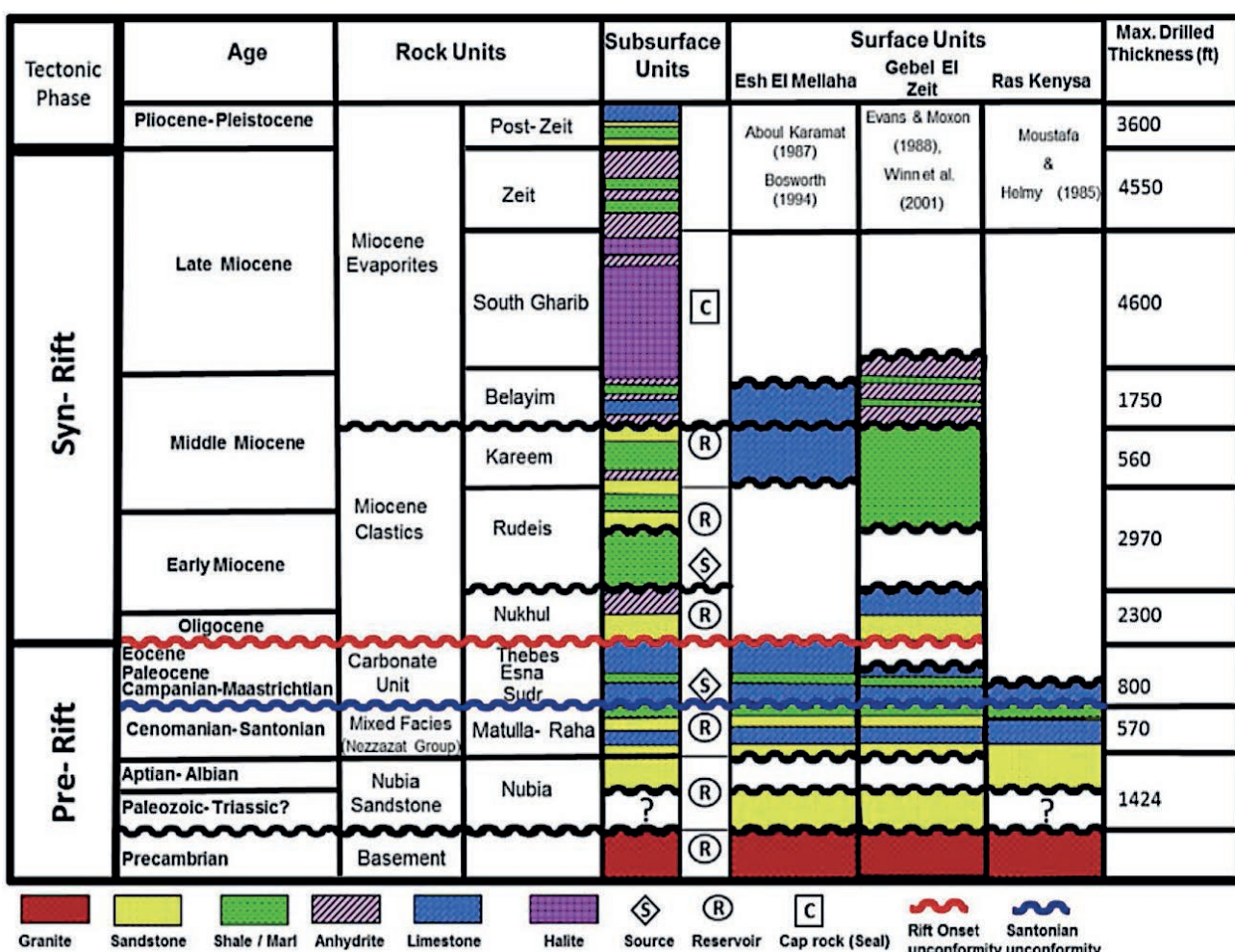


Figure 1.2. Lithostratigraphic geological column of southern Gulf of Suez including the study area of Gebel El Zeit after [33]
 Рисунок 1.2. Литостратиграфическая геологическая колонка южной части Суэцкого залива, включая район исследований Гебель-эль-Зейт по [33]

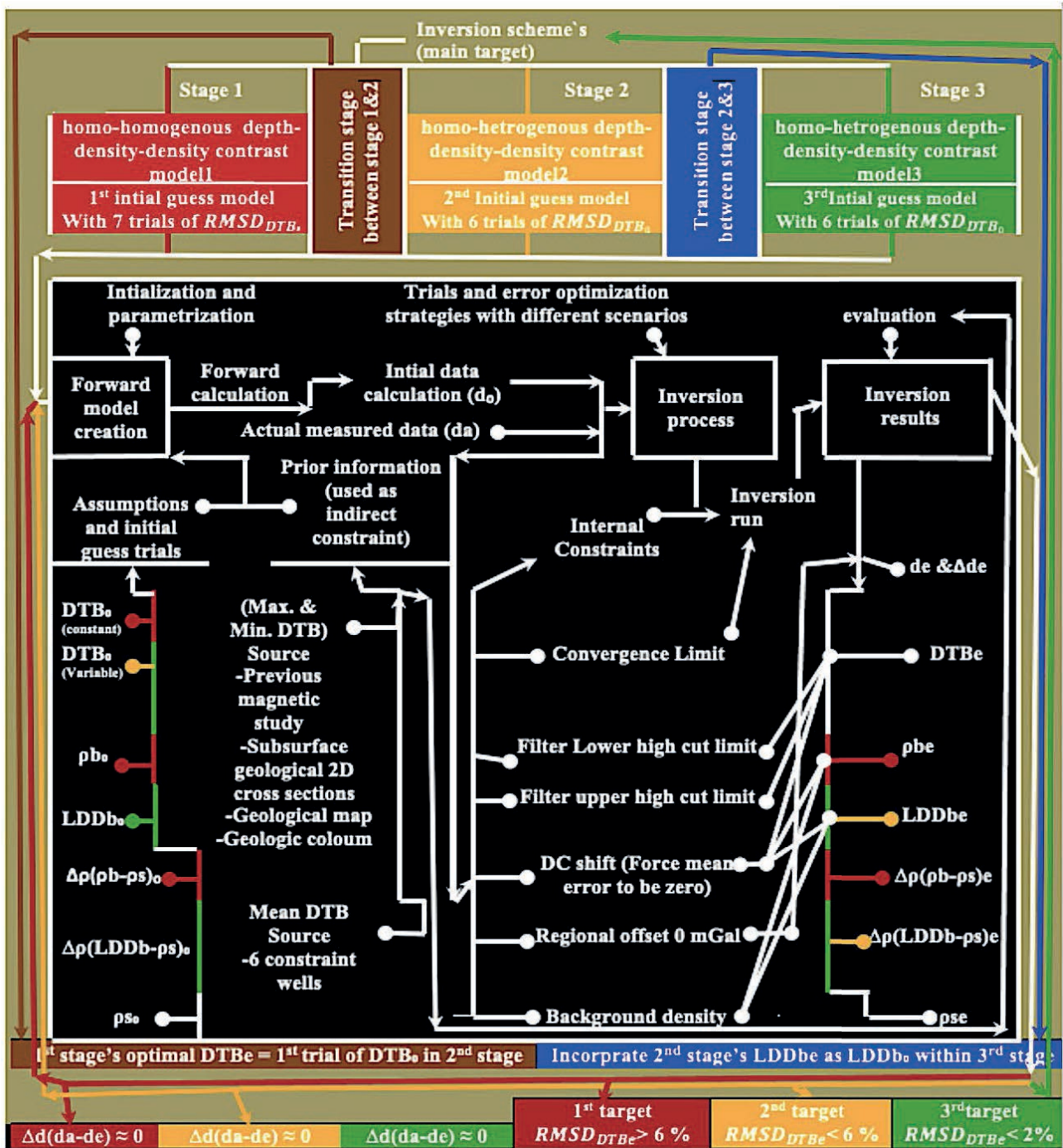


Figure 2.1. The flowchart for the three-stage inversion scheme used in the present research comprises optimization scenarios carried out at each stage and between stages. Tables 2.1 and 2.2 have a thorough list of abbreviations. Legend shown in figure 2.2
Рисунок 2.1. Блок-схема трехэтапной схемы инверсии, используемой в данном исследовании, включает сценарии оптимизации, выполняемые на каждом этапе и между этапами. В табл. 2.1 и 2.2 приведен подробный список сокращений. Легенда показана на рис. 2.2

diverged in the late Oligocene and early Miocene [21, 22]. Low-angle listric normal faulting and dyke injection created eastward half grabens along the rift's fault blocks [23]. The subsidence moved the rift axis eastward into the asymmetric axial grabens in the middle to late Miocene. During the Pliocene through the Pleistocene/Holocene, the southern Gulf of Suez intra-rift structural block Esh El-Mallaha was faulted and raised [24, 25]. As shown in fig. 1.1, *a*, Faults *F*1 and *F*2 follow the Gulf of Suez and run NW-SE in multiple wadis filled with Quaternary alluvium, juxtaposing Precambrian bedrocks

[26, 27]. Deep tectonic faults give the Gemsa-El Zeit Bay Basin a profound structural complexity. Nubian Sandstone, El Mallaha Formation, Raha Formation, Thebes Formation, Nukhul Formation, Lower/Middle Miocene Rudeis and Kareem layers, Sabkhas, and salt marshes comprise it [25, 28–31].

Metamorphic, granitic, and Dokhan volcanic rocks dominate the study area's eastern and western flanks, Gebels El Zeit and Esh El-Mallaha [32].

Gravimetry can enhance Earth model computations by investigating the potential field without the direct

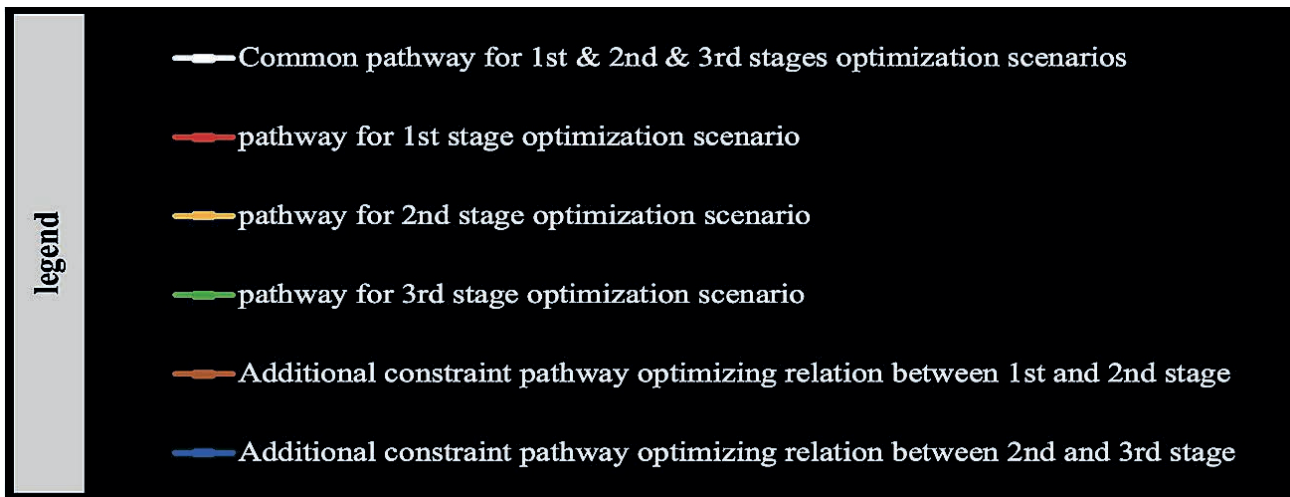


Figure 2.2. The legend for the proposed inversion scheme flow chart shown in figure 2.1
Рисунок 2.2. Легенда к предлагаемой блок-схеме схемы инверсии, представленной на рис. 2.1

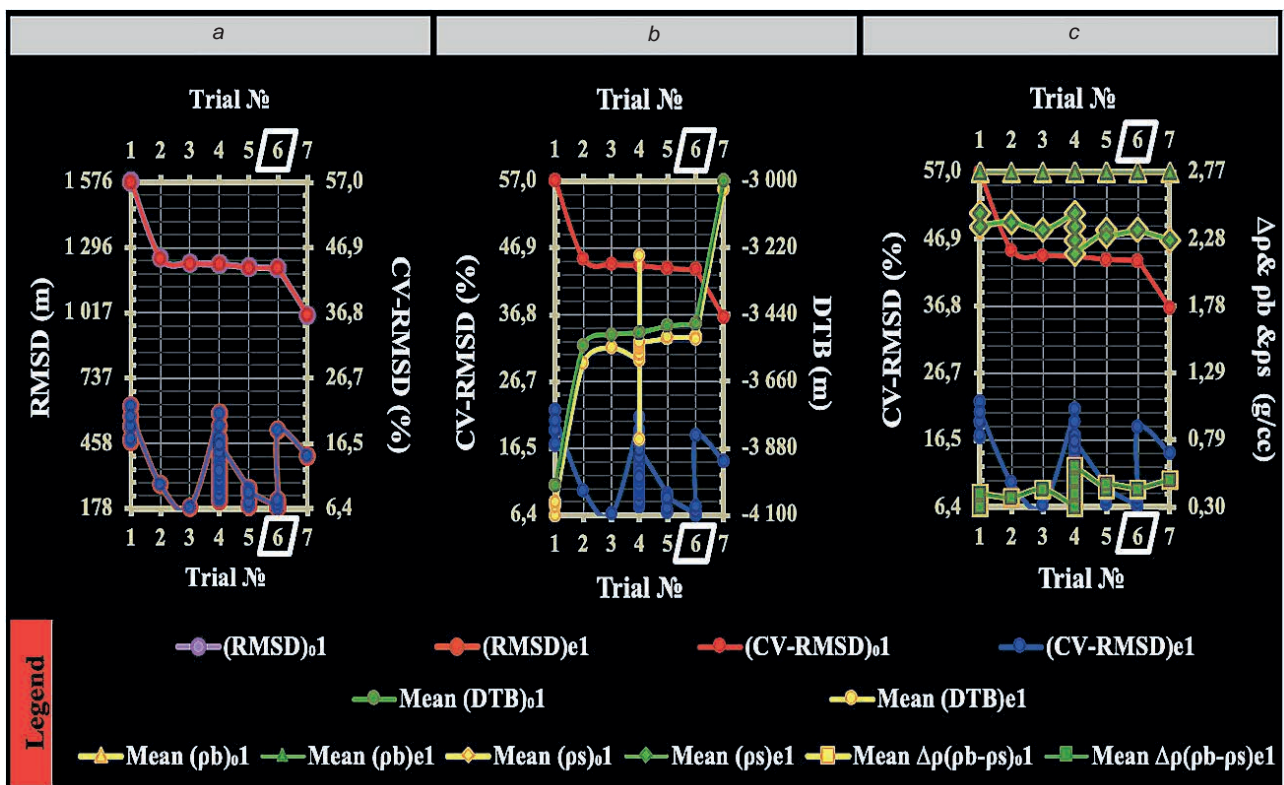


Figure 3. Three interconnected graphs (a–c) represent first-stage data analysis for depth inverse modeling in the inversion scheme. The y-axis in these graphs shows the first stage of initial guesses and inverse estimates of erroneous parameterization for modeling parameters, including basement depth, density, and density contrast. Initial depth error guesses seven trials on the x-axis controlled inverse estimation. The best solution was estimated on the sixth trial, with a 6.43 percent error. Tables 2.1 and 2.2 list abbreviations extensively
Рисунок 3. Три взаимосвязанных графика (а–с) представляют собой анализ данных первого этапа для глубинного инверсивного моделирования в схеме инверсии. По оси у на этих графиках показан первый этап исходных предположений и обратных оценок ошибочной параметризации параметров моделирования, включая глубину фундамента, плотность и контраст плотности. Начальная погрешность глубины предполагает семь попыток обратной оценки, контролируемой по оси x. Лучшее решение было оценено в шестом испытании с ошибкой 6,43 %. В табл. 2.1 и 2.2 подробно перечислены сокращения

constraint of stratigraphic-control wells. Table 1 lists these wells.

Bouguer gravity data. This study used a 0.01 mGal resolution Lacoste and Worden gravimeter (Scintrex Inc., USA). The Bureau Gravimetric International (BGI) in Paris

authorized the General Petroleum Corporation of Egypt's (GPC) ten-year (1974–1984) proposal to develop a gravity map of Egypt by establishing a national base net covering the whole country and augmenting all foreign companies' surveys. The Egyptian Academy of Scientific Research and Technology

supervised it. Remeasurements ensured correctness. Raw data were exported in x , y , and z dimensions, gridding at 1000 m intervals.

The contour map of the research area was colored using Bouguer anomalies (Fig. 1.1, b). Remarkable doublet Western gravity highs suggest local transfer faults intersect Gebel Esh El-Mallaha. Gebel El Zeit and Esh El-Mallaha display complicated basement outcrops east and west of Gemsa-El Zeit Bay, with a vast sedimentary basin in the middle as shown in fig. 1.1, a, b, c.

The Litho-stratigraphic geological column of southern Gulf of Suez including the study area of Gebel El Zeit is represented in fig. 1.2 [33].

Inversion Scheme

General Outline. Douglas Oldenburg and others in the three-stage inversion scheme quantified the El-Zeit basin's geologic attributes. The Oasis Montaj program's GM-SYS extension sub-routine (Geosoft Inc., Toronto, ON, Canada) uses a popular spectral layered-earth inversion algorithm for data reduction, filtering, and optimization, resulting in the best inversion solution for basement relief delineation. It also determines the appropriate average density for the sedimen-

tary-basement layers, their density difference, depths to the basement, and sedimentary section thickness under the study area. Its inversion results were compared to others to establish if Oldenburg's constraining parameters produced the best-solved and most reliable model. For time and effort reduction, the proposed inversion scheme employs a basic forward model and six optimization strategies to obtain the optimal initial and inverse models, three from forward modeling and three from inverse modeling. The parameterization flowchart for the proposed scheme's forward and inverse modeling operations is shown in fig. 2.1 with a legend in fig. 2.2, and all parameterization abbreviations utilized within our research are listed in tables 2.1 and 2.2.

Stages of the Scheme. In the first stage, three optimization strategies have been proposed: one for forward depth modeling that uses the unconstrained initial forward constant mean depth surface within the 3D depth model guess trials; another for forward density modeling that uses the initial forward density constraint assumptions of the 3D homogenous two-layered density model guess trials; and a third for depth inverse modeling that incorporates both of those for recovering Oldenburg's model with the lowest possible error.

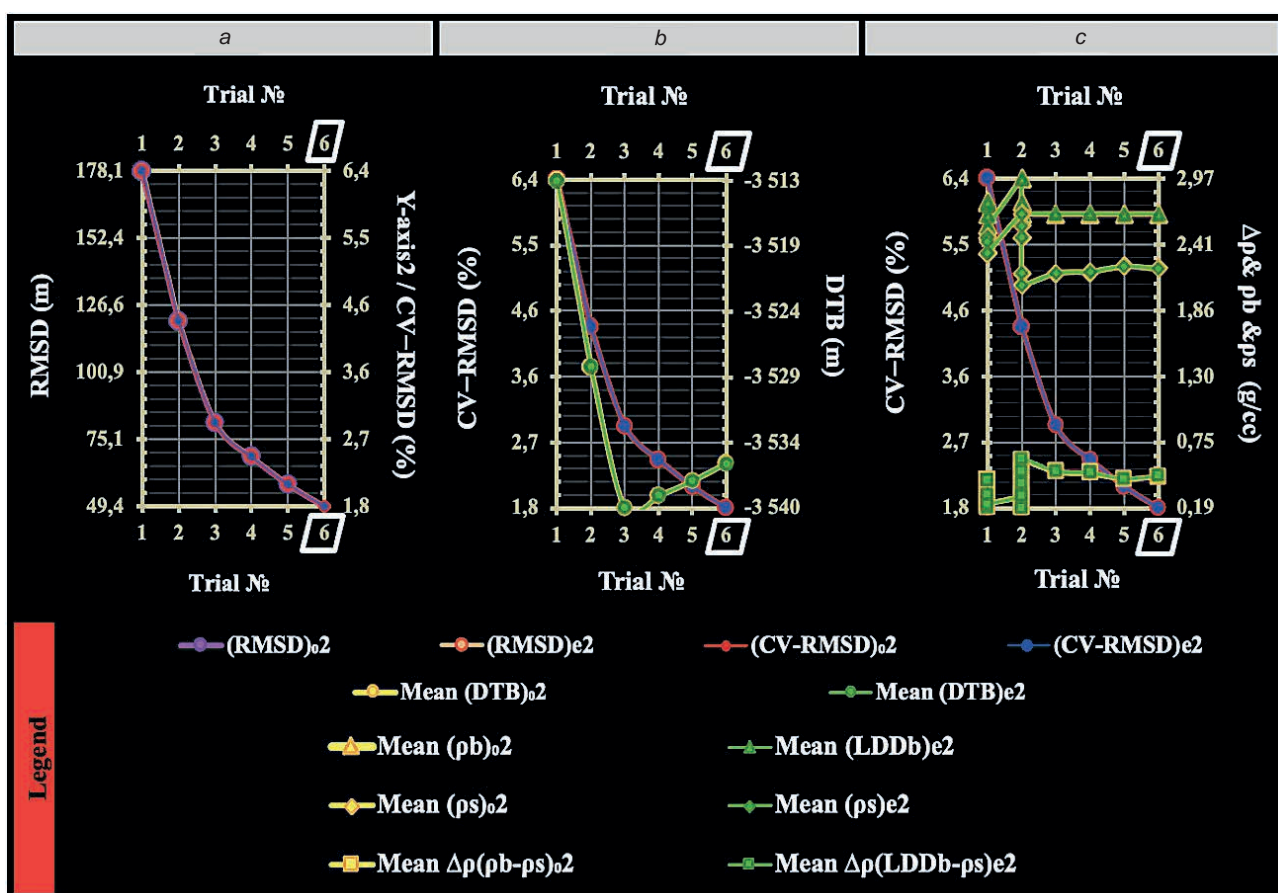


Figure 4. Three interconnected graphs (a–c) show the second-stage data analysis for density inverse modeling in the inversion scheme. These graphs show the second stage of initial guesses and inverse estimates of erroneous modeling parameterization for basement depth, density, and density contrast on the y-axis. Initial depth error guesses seven trials on the x-axis controlled inverse estimation. With a 1.87 percent error, the sixth trial's optimal solution was likely depth-constrained. Tables 2.1 and 2.2 list all abbreviations.

Рисунок 4. Три взаимосвязанных графика (а–с) показывают анализ данных второго этапа для моделирования инверсионной плотности в схеме инверсии. Эти графики показывают второй этап исходных предположений и обратных оценок ошибочной параметризации моделирования глубины фундамента, плотности и контраста плотности по оси у. Начальная погрешность глубины предполагает семь попыток обратной оценки, контролируемой по оси х. С ошибкой в 1,87 % оптимальное решение шестого испытания, вероятно, было ограничено по глубине. В табл. 2.1 и 2.2 перечислены все сокращения

In the second stage, three further optimization strategies are proposed: One is forward depth modeling, where the initial forward variable depth surface has been used within the 3D depth model guess trials with varying depth guessing errors, imposing error reduction constraint assumptions from trial to trial for parameterization sequences' constraining; another strategy for forward density modeling that applies constraints to the density contrast guess trials of the initial 3D constant mean density contrast interface is to separate several guess trials of a homogeneous two-layered density model; and a third for density inverse modeling that incorporates both of those second stage's aforementioned forward strategies for recovering the densities best possible solutions.

The third final stage used three additional optimization strategies: one for forward depth modeling, which uses an unconstrained version of the forward variable depth constraint assumptions derived from the trials of inverted 3D possible depth models with varying errors in depth calculations; another for forward density modeling, which uses the constrained version of second stage's inverted lateral density possible models; and third strategy for the inverse depth modeling, which makes use of these constraint versions sought to evaluate the best possible density and density contrast model solutions,

leading to the best possible basement depth model solution with the minimal inaccuracies. We achieved this low error by repeatedly refining depth-density model solutions inside the density contrast constrained-unconstrained optimization scenario between the second and third stages of the proposed inversion approach.

Results and discussion

A Comparison of the best-possible models in three stages. We identified that for three best-possible forward models, we could obtain three best-possible inverse models, resulting in minimal error optimal solutions constrained by the three initial best-possible mean depth error guessing trials, as highlighted in fig. 3, 4, 5. Each stage uses a different strategy to generate forward models and locate their matching inverse solutions. The model's optimality in minimizing calculational error validated its reliability and efficacy based on an inversion results analysis conducted on the entire study area and individual locations.

These forward models were started with the optimal forward initial parameterization guessing sequences, which included these parameters for the first stage: Z_0 -3470 m, ρ_b 2.77 g/cc, ρ_s 2.34 g/cc, $\Delta\rho(\rho_b-\rho_s)_0$ 0.43 g/cc, Δd_0 37.65 mGal, D_c shift 37.652 mGal, filter LHC limit 14000 m, filter UHC limit 7500 m, convergence limit 0.01 mGal, and regional offset

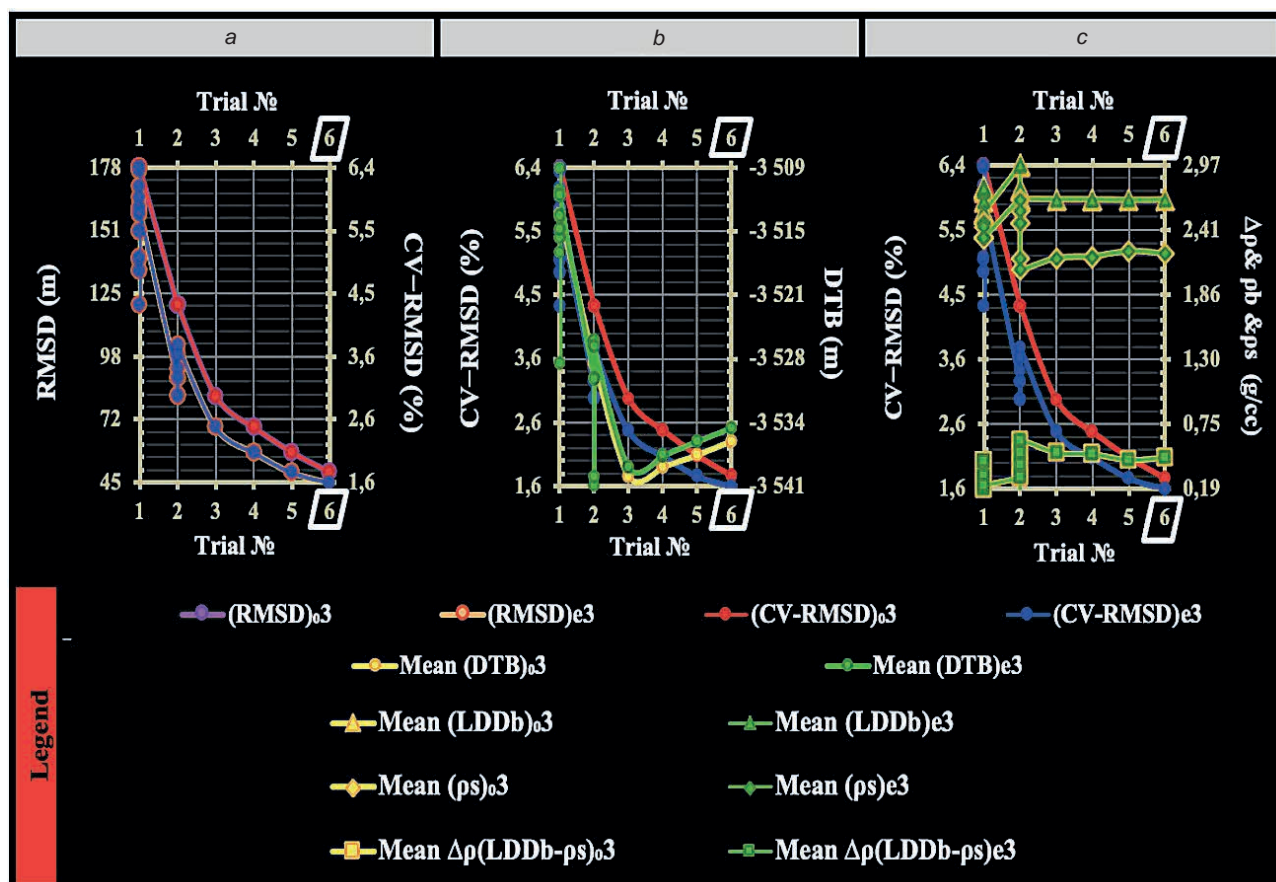


Figure 5. Three interconnected graphs (a–c) show the third-stage data analysis for depth inverse modeling in the proposed inversion scheme. These graphs show the third stage of initial guesses and inverse estimates of erroneous modeling parameterization for basement depth, density, and density contrast on the y-axis. Initial depth error guesses seven trials on the x-axis controlled inverse estimation. With a 1.63 percent error, the sixth trial's optimal solution was optimally estimated. Tables 2.1 and 2.2 list all abbreviations

Рисунок 5. Три взаимосвязанных графика (а–с) показывают анализ данных третьего этапа для глубинного инверсионного моделирования в предлагаемой схеме инверсии. Эти графики показывают третий этап исходных предположений и обратных оценок ошибочной параметризации моделирования глубины фундамента, плотности и контраста плотности по оси у. Начальная погрешность глубины предполагает семь попыток обратной оценки, контролируемой по оси х. С ошибкой 1,63 % оптимальное решение шестого испытания было оценено оптимально. В табл. 2.1 и 2.2 перечислены все сокращения

0 mGal. These inputs started the forward modeling guesswork process with 43.6% inaccuracy. For the second stage, these parameters were included: Z_0 –3536 m, ρb_0 2.67 g/cc, ρs_0 2.21 g/cc, $\Delta\rho(\rho b-\rho s)_0$ 0.46 g/cc, Δd_0 42.661 mGal, Dc shift 42.661 mGal, filter LHC limit 10000 m, filter UHC limit 9600 m, convergence limit 0.0054 mGal, and regional offset 0 mGal, with 1.78% error in forward modeling guessing. Finally, for the third stage, these parameters were included: Z_0 –3536 m, $LDDb_0$ 2.6706 g/cc, ρs_0 2.21 g/cc, $\Delta\rho(LDDb-\rho s)_0$ 0.4606 g/cc, Δd_0 42.670 mGal, Dc shift 42.670 mGal, filter LHC limit 20000 m, filter UHC limit 15000 m, convergence limit 0.0001 mGal, and regional offset 0 mGal, with 1.78% error in forward modeling guessing.

The estimated parameters recovered the first stage's optimal inverse model as follows: Ze –3513 m, ρbe 2.77 g/cc, ρse 2.34 g/cc, $\Delta\rho(\rho b-\rho s)e$ 0.43 g/cc, Δde 0.0506 mGal, Dc shift 37.652 mGal, filter LHC limit 14000 m, filter UHC limit 7500 m, convergence limit 0.01 mGal, and regional offset 0 mGal. These parameters were estimated with a 6.4% error. Second, recovered the second stage's optimal inverse model by this sequence (Ze –3536 m, $LDDbe$ 2.6706 g/cc, ρse 2.21 g/cc, $\Delta\rho(LDDb-\rho s)$ e 0.4606 g/cc, Δde 0.0094 mGal, Dc shift 42.661 mGal, filter LHC limit 10000 m, filter UHC limit 9600 m, convergence limit 0.0054 mGal, and regional offset 0 mGal), with 1.78 % estimation error. Finally, recovered the third stage's optimal inverse model by this sequence (Ze –3534.6 m, $LDDbe$ 2.6706 g/cc,

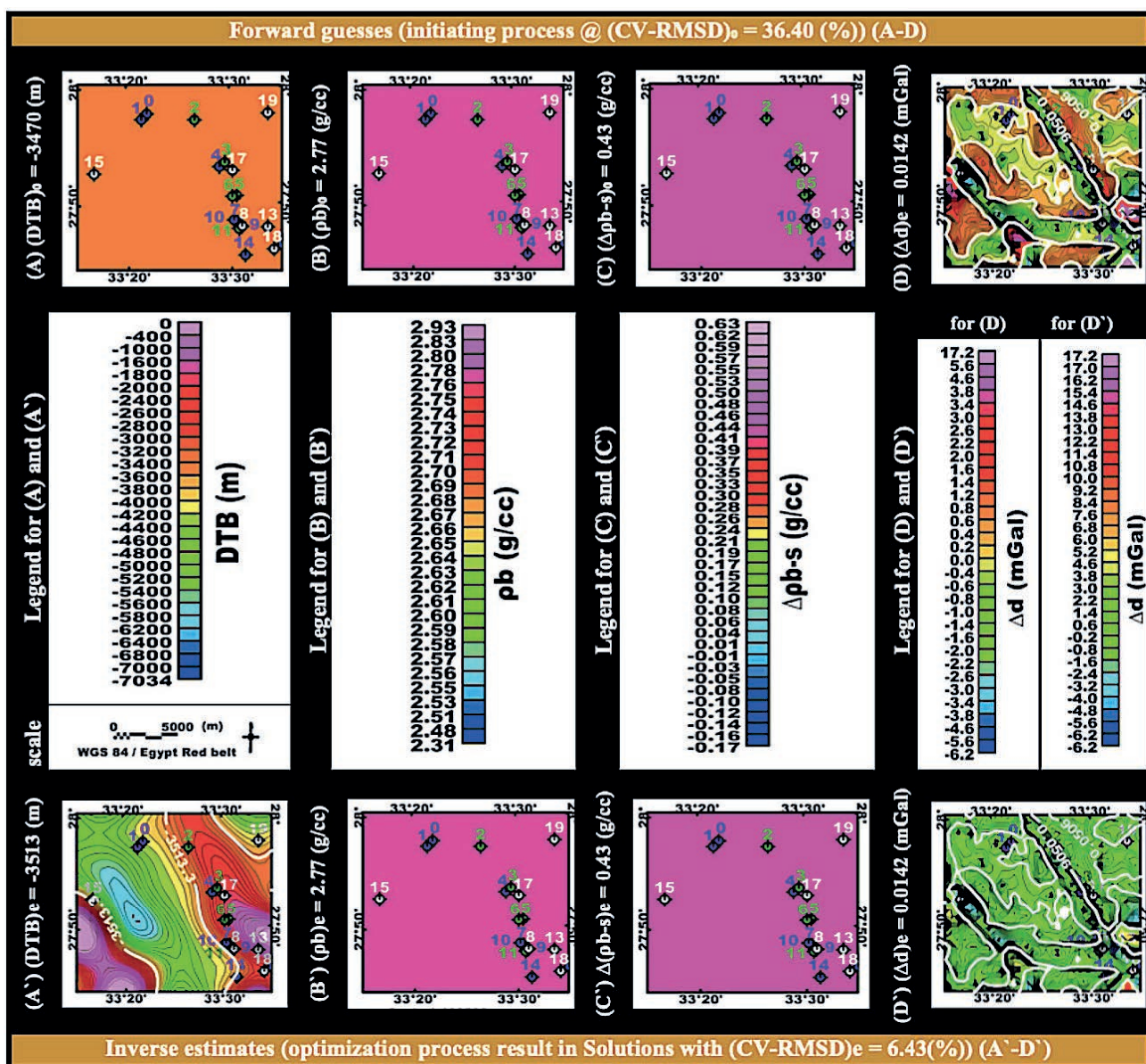


Figure 6. The first stage of the inversion scheme involves making optimal forward guesses and inverse estimates for four parameters: DTB , ρb , $\Delta\rho b-s$, and Δd . These parameters relate to the complex basement depth (maps A and A'), density (maps B and B'), and density contrast interface with the overlaid sediment layer (maps C and C'), as well as the data misfit residual Bouguer anomalies (maps D and D'). All maps for each parameter share the same legend and scale

Рисунок 6. Первый этап схемы инверсии включает в себя получение оптимальных прямых предположений и обратных оценок для четырех параметров: DTB , ρb , $\Delta\rho b-s$ и Δd . Эти параметры относятся к комплексной глубине фундамента (карты A и A'), плотности (карты B и B') и границе контраста плотности с перекрытым слоем осадочных пород (карты C и C'), а также данные, не соответствующие остаточным аномалиям Буге (карты D и D'). Все карты для каждого параметра имеют одну и ту же легенду и масштаб

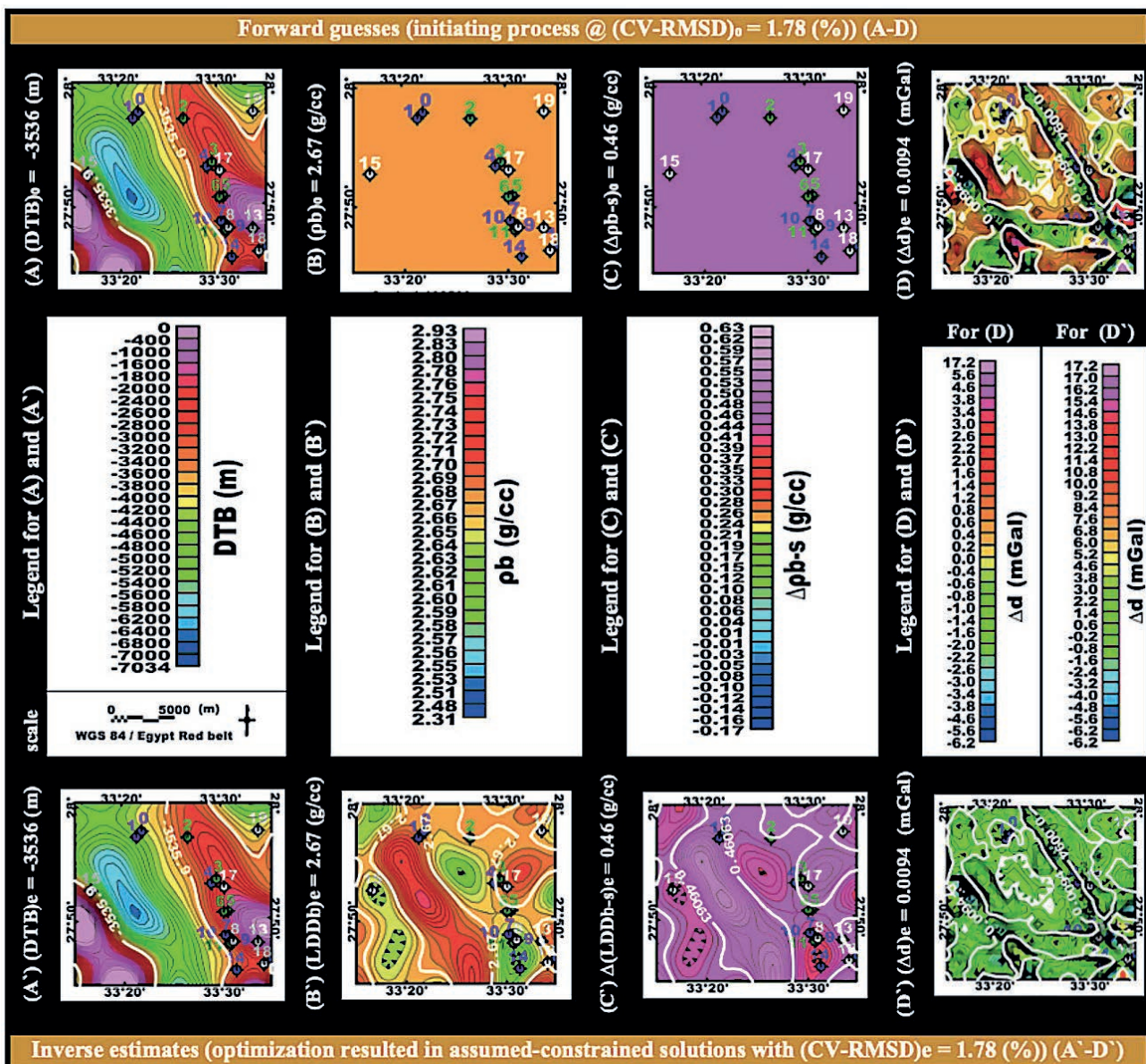


Figure 7. The inversion scheme's second-stage initial parameterizations and their optimally estimated best-possible inverse estimates of the basement depth (maps A and A'), complex basement density (maps B and B'), basement-sediment density contrast interface (maps C and C'), and data misfit residual Bouguer anomalies (maps D and D'). The forward guess and inverse estimate maps have the same legend for each parameter to facilitate comparison

Рисунок. 7. Начальные параметризации второго этапа схемы инверсии и их оптимально оцененные наилучшие обратные оценки глубины фундамента (карты A и A'), комплексной плотности фундамента (карты B и B'), границы контраста плотности фундамента и отложений (карты C и C') и данные, не соответствующие остаточным аномалиям Буге (карты D и D'). Карты прямого предположения и обратной оценки имеют одинаковую легенду для каждого параметра, чтобы облегчить сравнение

pse 2.21 g/cc, $\Delta\rho(LDDb-\rho_s)e$ 0.4606 g/cc, Δde 0.0045 mGal, Dc shift 42.670 mGal, filter LHC limit 20000 m, filter UHC limit 15000 m, convergence limit 0.0001 mGal, and regional offset 0 mGal), with 1.63% estimation error.

We subsequently linked the three-stage best-possible inverse parameterization estimates and their errors to assess our scheme's overall optimality in minimizing computational error within this gradual improvement (first, 6.4; then, 1.78; finally, 1.63%) from the first to the third stage. This error sequence resulted from iteratively optimizing in the presence of zero regional offsets used as a data-misfit constraint within the three stages, the mean depth key parameter (first, -3513; then, -3536; finally, -3534.6 m), the mean density contrast key parameter (0.43; 0.4606; 0.4606 g/cc), the filter LHC limit constraint parameters

(14000; 10000; 20000 m), the filter UHC limit constraint parameters (7500; 9600; 15000 m), the convergence limit constraint parameter (0.01; 0.0054; 0.0001 mGal), and the DC shift constraint parameter (37.652; 42.661; 42.670 mGal).

Quantitative interpretation. Fig. 6, 7, 8 show the best forward initial guesses and inverse estimates for the proposed inversion scheme's first, second, and third stages. Using a quantitative interpretation of the inverse outcomes, we were able to conclude the following about the optimality of the key and constraint model parameters that make up the inverse optimal parameterization sequence in the inversion scheme's third-last stage:

- As illustrated in maps A and A' in fig. 8, the third stage's optimal inversion process's initial forward depth model

with guessing parameters of Mean DTB_0 –3535.9, Max. DTB_0 –6460.9, Min. DTB_0 0, and SD DTB_0 1564.8 m, with an initial depth inaccuracy of 1.78%, yielding the most optimal inversely estimated depth parameters of (Mean $DTBe$ –3534.6, Max. $DTBe$ –6453.2, Min. $DTBe$ 0, and SD $DTBe$ 1567.4 m) estimated with a 1.63% depth error. The forward initial mean depth parameter (Mean DTB_0 = –3535.9 m) is the closest approximation to the optimal basement mean depth (Mean $DTBe$ = –3534.6 m) in the study area. Map A's basement geological alteration demonstrates that two primary normal faults from the surface to considerable depths created the Graben system underneath the study area. The outcropping basement rocks in the geological map fit the second-best depth parame-

ter (Min. $DTBe$ = 0 m). The third-best maximum depth model parameter shows that the two main normal faults extend to –6453.2 meters below sea level in the middle basinal area. Minor faults run alongside the primary southeast-to-northwest normal faults on both sides of the central graben. The basement complex's two normal faults generated the huge sedimentary basin between the eastern El-Zeit and western Esh El Mallaha mountain ranges in the study area.

2. Third stage of our inversion scheme's optimal inversion process started with optimal initial forward density guessing parameters of (Mean $LDDb_0$ 2.6706, Max. $LDDb_0$ 2.7558, Min. $LDDb_0$ 2.5935, and SD $LDDb_0$ 0.0294 g/cc) as a 1.74% error constraint assumption, resulting in the best possible

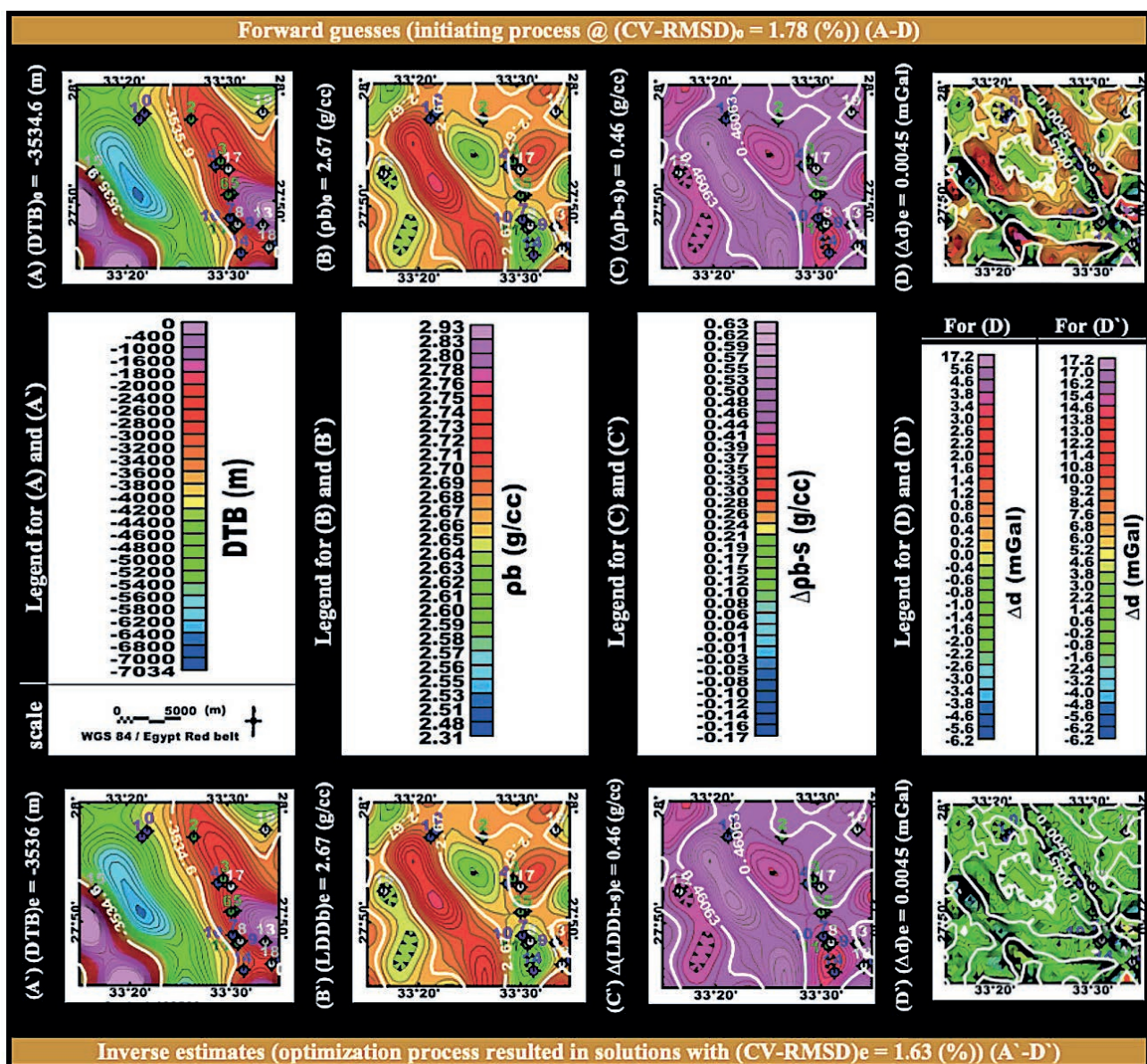


Figure 8. Our inversion scheme's last third stage optimally initiated forward guesses and their resultant optimal estimates for four parameters with a 1.63% error in the estimation of the basement depth (maps A and A'), the complex basement density (maps B and B'), the basement-sedimentary density contrast interface (maps C and C'), and the data misfit residual Bouguer anomalies (maps D and D'). For ease of comparison, each parameter's forward-guessed and inversely estimated maps share the same legend

Рисунок 8. Последний третий этап нашей схемы инверсии оптимально инициировал упреждающие предположения и их суммарные оптимальные оценки для четырех параметров с ошибкой 1,63% в оценках глубины фундамента (карты A и A'), комплексной плотности фундамента (карты B и B'), границы контраста плотности фундамента и осадочных пород (карты C и C') и несответствия данных остаточным аномалиям Буге (карты D и D'). Для простоты сравнения карты каждого параметра с прямой и обратной оценкой имеют одну и ту же легенду

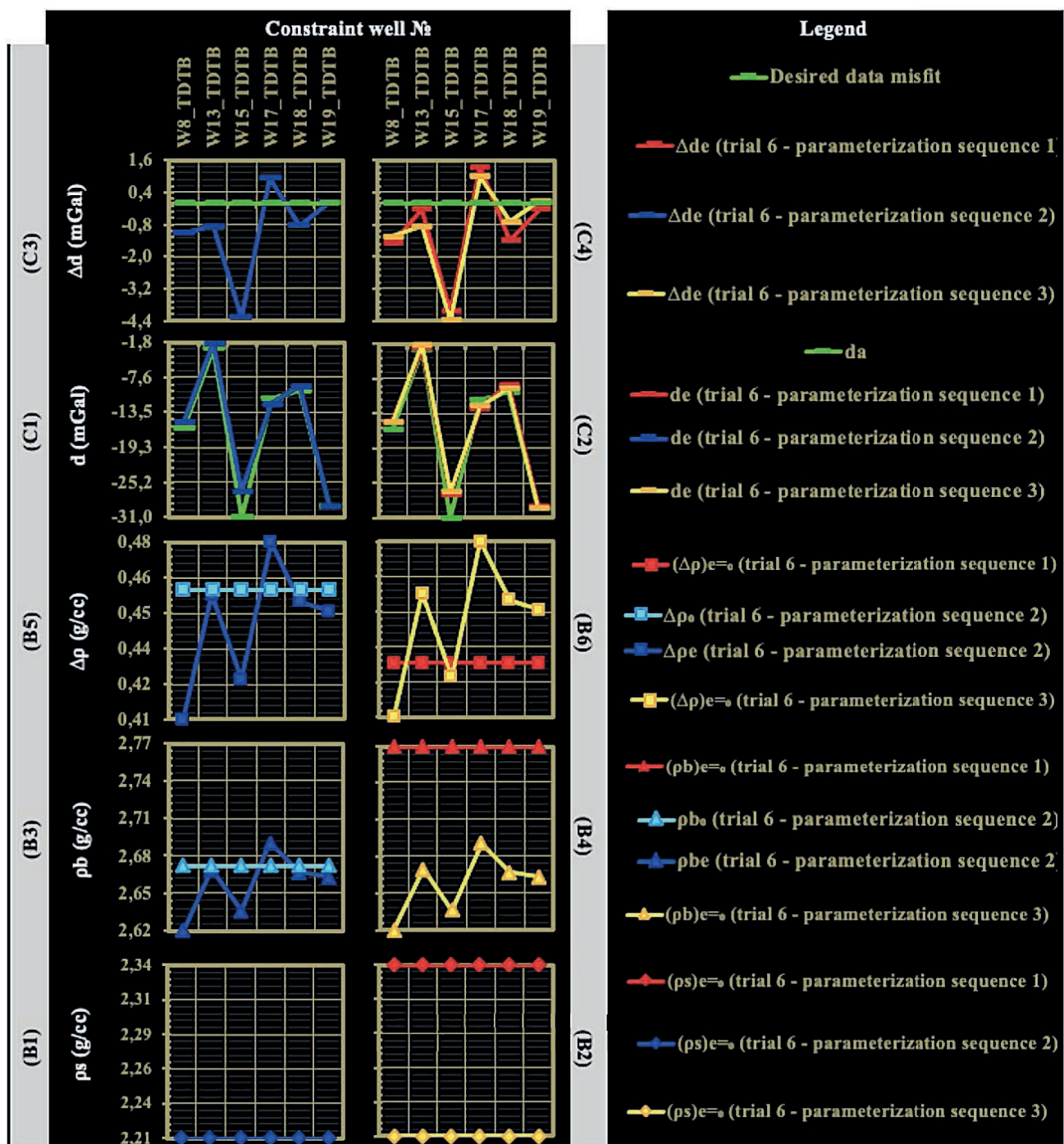


Figure 9.1. Continued in figures 9.2
Рисунок 9.1. Продолжение на рис. 9.2

constrained density parameters of Mean $LDDbe$ 2.6706, Max $LDDbe$ 2.7558, Min $LDDbe$ 2.5935, and $SD LDDbe$ 0.0294 g/cc. These estimates produced a density solution with a default 1.63% computed depth inaccuracy. The initial 2.6706 mGal mean density parameter on Map B' in fig. 8 suggests that granitic basement rocks dominate the basement complex's lateral mean density distribution in the study area. The second and third $LDDbe$ density parameters (minimum 2.5935 and maximum 2.7558 g/cc) describe acidic igneous rock densities in which the basement depth laterally confines and best matches prior information. Working in that density space helps recover the optimal inverse estimated depth model. Basement rocks outcrop at zero depth (Fig. 8), map B' .

3. In addition, the basement-sedimentary interface in the study area has been interpreted as a density contrast constraining assumption within the optimal sixth inverse depth modeling trial of our inversion scheme's third stage, with the following parameters: Mean 0.4606, Max 0.5458, Min 0.3835, and SD 0.0294 g/cc. The optimal initialized forward modeling, incorporating initially limited forward density contrast parameters (Mean 0.4606, Max 0.5458, Min 0.3835, and SD 0.0294 g/cc), yielded these optimum inverse density contrast assumptions. As shown in Map C' of fig. 8, the mean lateral density contrast (Mean $\Delta \rho(LDDb - ps)$ 0.4606 g/cc) was confined to optimize distribution on the sedimentary section-basement complex interface in the research area, with maximum and minimum

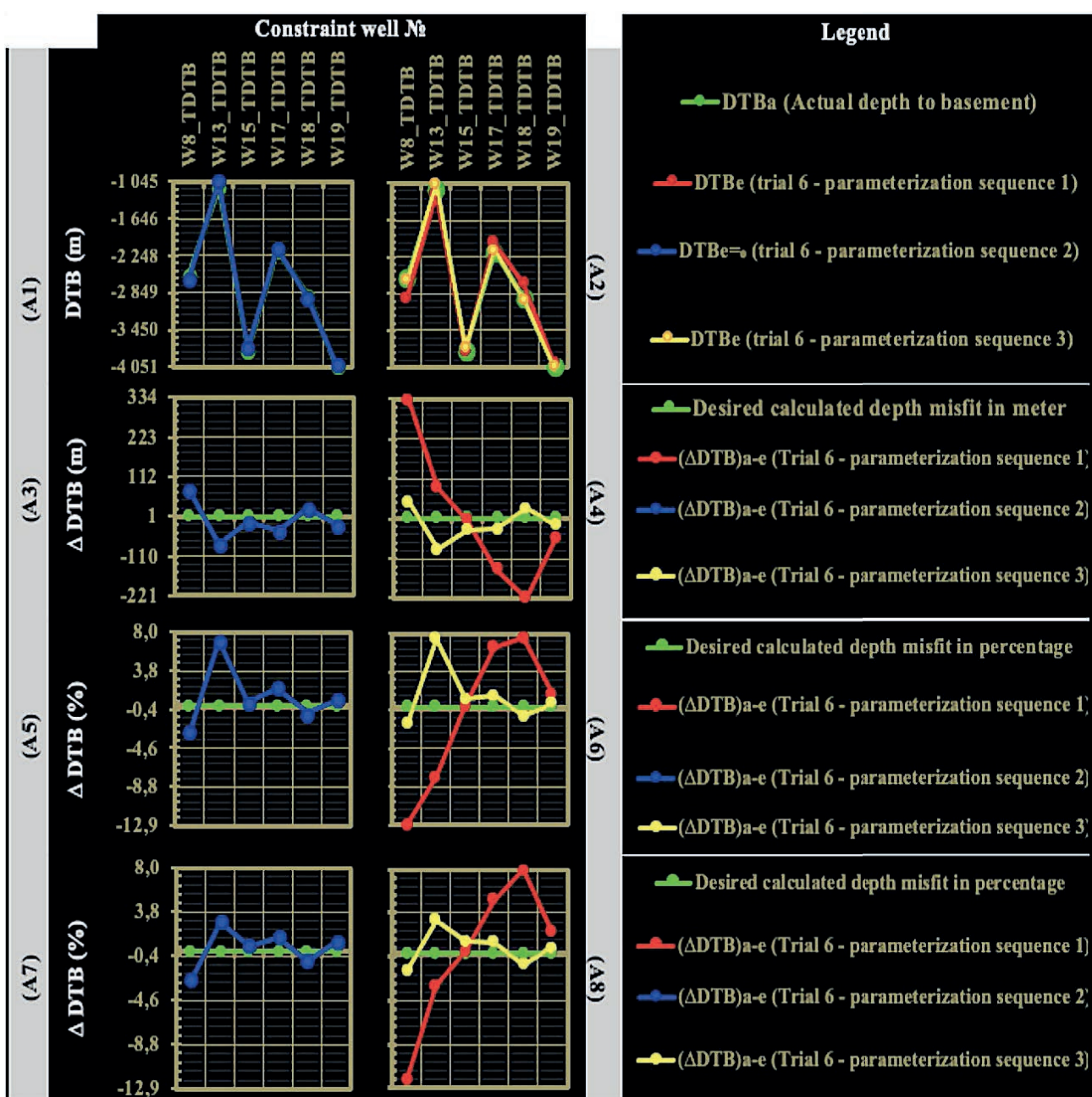


Figure 9.2. An extension of the preceding figure 9.1, together illustrating the three-stage inversion scheme's six basement total depth constraint wells' focused data analysis (shown in figures 9.1 and 9.2) illustrates the indirect constraining process of the three best-possible models' solutions for the entire research area. Checks for quality control tests ensure that the best outcomes correspond as closely as possible to real constraints and desired solutions. The red, blue, and yellow sequences indicate the first, second, and third best-possible solutions. Green circles represent the quality solutions that are desired. Tables 2.1 and 2.2 have a thorough list of abbreviations

Рисунок 9.2. Расширение предыдущего рис. 9.1, иллюстрирующее анализ данных шести скважин с ограниченной глубиной фундамента трехступенчатой схемы инверсии (показанной на рис. 9.1 и 9.2), иллюстрирует процесс косвенного ограничения решений трех наилучших моделей для всей области исследований. Проверки по контролю качества гарантируют, что наилучшие результаты максимально соответствуют реальным ограничениям и желаемым решениям. Красная, синяя и желтая последовательности обозначают первое, второе и третье наилучшие возможные решения. Зеленые круги обозначают желаемые качественные решения. В табл. 2.1 и 2.2 приведен подробный список сокращений

bounds of 0.5458 and 0.3835 g/cc, respectively. These optimized density contrast parameters and its best constraint assumption at the interfaced surface provided an optimal El-Zeit sedimentary-basement basinal depth model in the study area with a mean minimum error of 1.63% in delineations.

4. We investigated the data-misfit parameters (Mean 0.0045, Max 14.2795, Min -4.9724, and SD 1.3111 mGal) to in-

terpret the optimal model's Bouguer response. Fig. 8 illustrates the lateral distribution of linear and normal-colored Bouguer anomalous misfits after recovering the optimal inverse-estimated model's solutions. Map D's linear color legend shows the minimal mean data misfit estimations of 0.0045 mGal, covering practically the whole study area between estimated and observed Bouguer anomalies with means of $de = -24.9139$

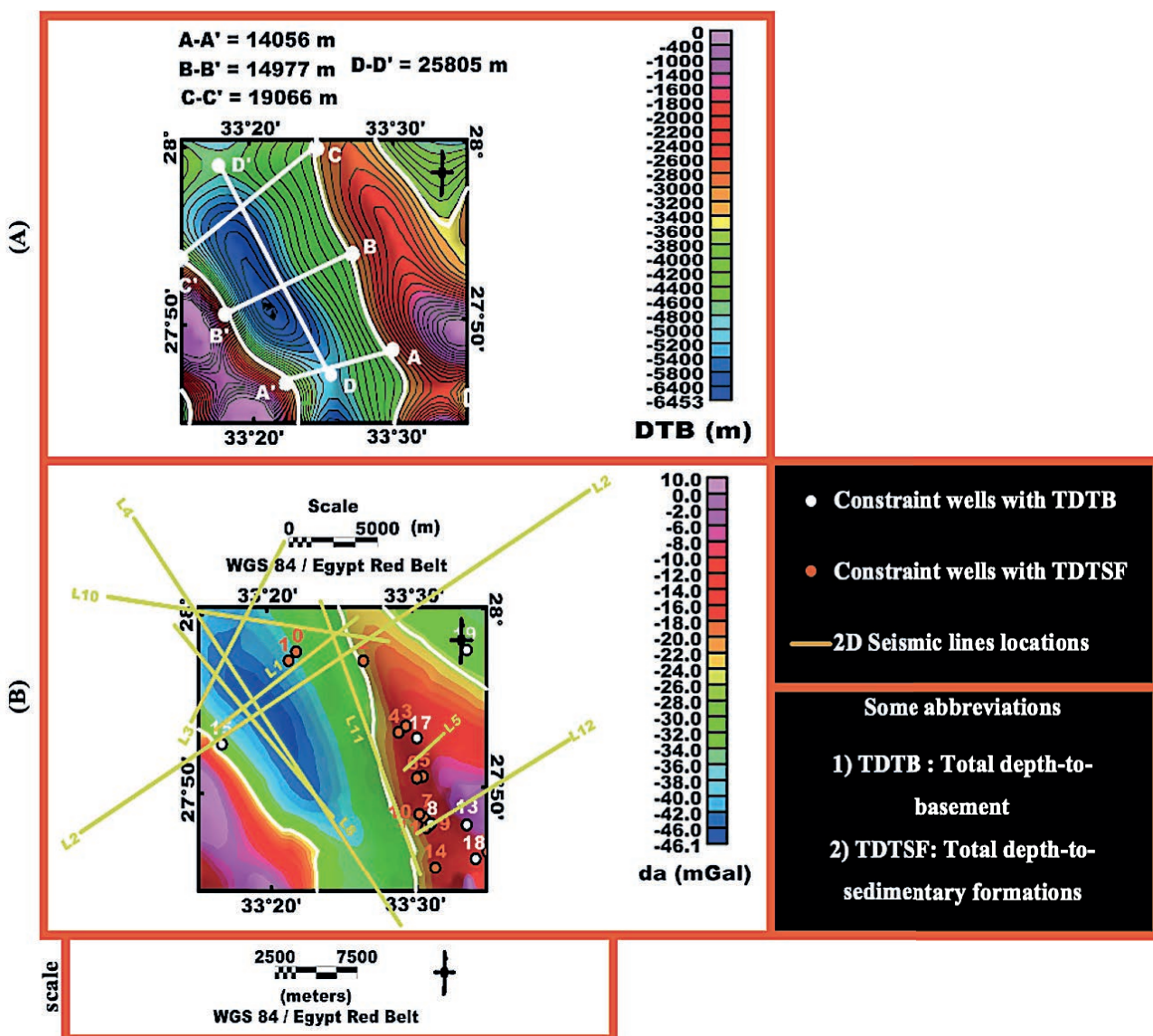


Figure 10.1. Continued in figures 10.2
Рисунок 10.1. Продолжение на рис. 10.2

and $da = -24.9094$. The mean Bouguer anomaly's misfit optimality is bounded by 14.2795 and -4.9724 mGal. Map D in Fig. 7 shows how the substructure of elongated basins in the sedimentary layer above the basement complex along two significant normal faults provided the first viable migration and oil accumulation zones. These extended basins produced low Bouguer anomalies on Map D. These basins formed when the graben system's two main normal faults squeezed sedimentary layers over a basement complex. Over the middle El-Zeit basin, fault compression forms subsidiary sedimentary basins.

5. These best constraint parameters of Dc shift 42.6709 mGal, filter LHC limit 20 000 m, filter UHC limit 15 000 m, convergence limit 0.0001 mGal, and regional offset 0 mGal maximally constrained the third last stage's inverse-estimated parameterization sequence's optimality, resulting in the optimal model's minimal errored solutions. The first constraint parameter (DC shift = 42.6709 mGal) was utilized to predict the forward initial mean depth parameter (Mean $DTB_0 = -3536$ m), estimating the inverse mean depth parameter (Mean $DTBe = -3534.6$ m). The second constraint parameter (filter LHC limit

= 20 000 m) smoothed the optimal inverse-estimated mean density-depth model and its calculated mean Bouguer anomaly response. The third constraint parameter (filter UHC limit = 15 000 m) optimized the impact of the second constraint. The second and third parameters govern the model's solution and their data calculation smoothness and non-smoothness. The calculated and observed Bouguer anomalies are best fit with a mean misfit $\Delta de = 0.0045$ mGal when the fourth regional offset constraint parameter is zero after recovering the optimal inverse model's solutions in the study area. The inversion run stops when the standard deviation difference between the last two iterations' data misfit is less than the fifth convergence limit parameter, which equals 0.0001 mGal. The fourth and fifth constraint parameters help estimate the optimal inverse model solution with minimal computational errors.

Evaluation of the inversion stages

Through indirect analysis of drilled-well data

1 & 2. Fig. 9.1 and 9.2 show constraint wells for quality control and optimal inversion solution testing. The study area

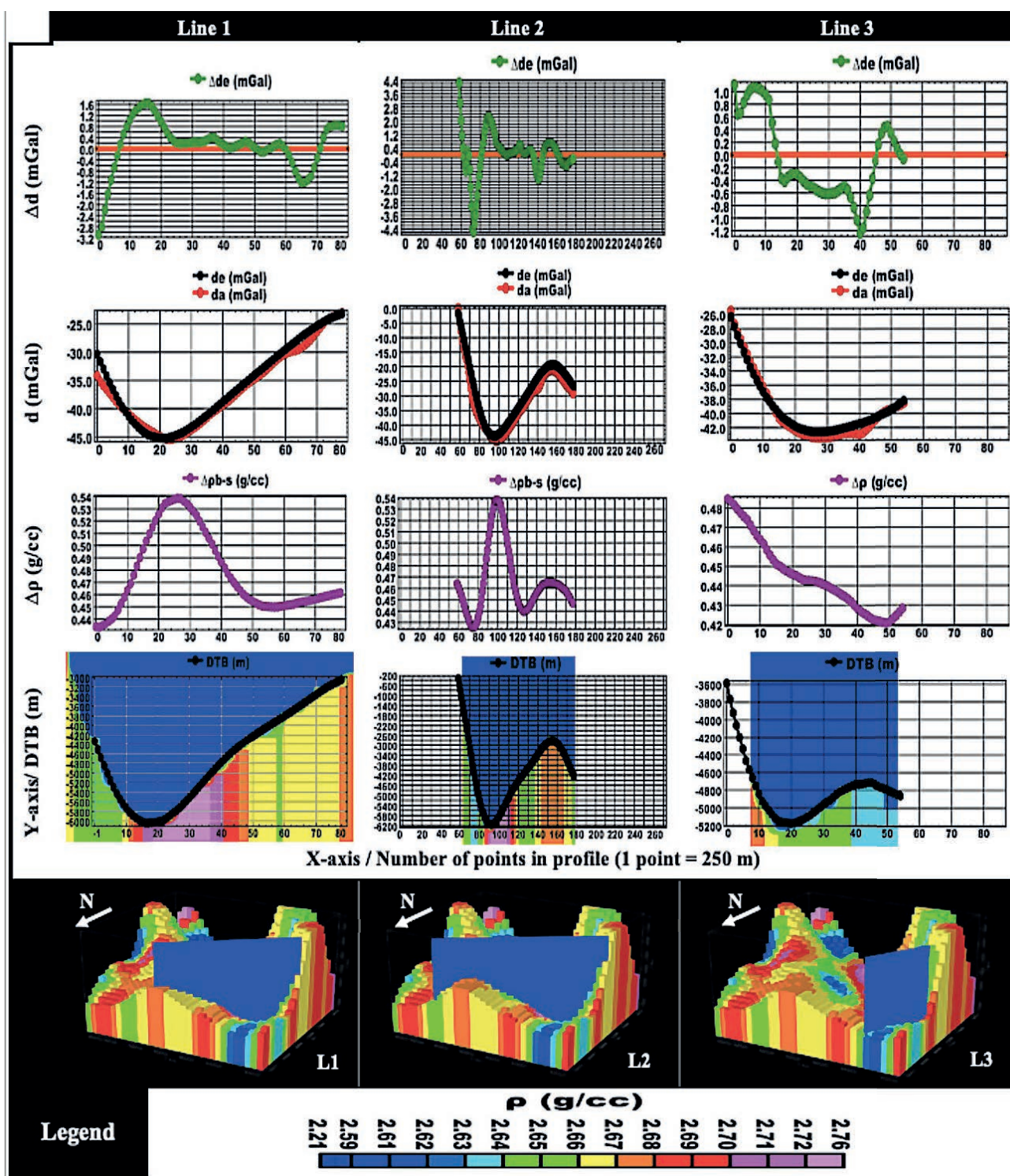


Figure 10.2. Continuation of figure 10.1. Continued in figures 10.3
Рисунок 10.2. Продолжение рис. 10.1. Продолжение на рис. 10.3

had nineteen wells, and a gravity inversion was used to get the optimal 3D basement estimated depth. The DC shift, convergence limit, regional offset, and filter lower and upper high cut limits were adjusted to manage the misfits of calculated data and model solutions from the constraints of actual measured values. After inversion, basement constraint wells were used as a first quality control test to ensure the inverse depth values stayed inside the analytic depth domain. As a second quality control, we checked whether the optimal inverted depth to the

basement was more profound than the total depth of the thirteen unreachable basement constraint wells.

Indirect usage of the first and second controls reflects a forward-initiated unconstrained model without strong depth constraints, inverting the lateral 3D optimal final depth solution with minimal error. This strategy works better with less prior information and considers applying the proposed inversion scheme to a new domain requiring more data for reliable predictions.

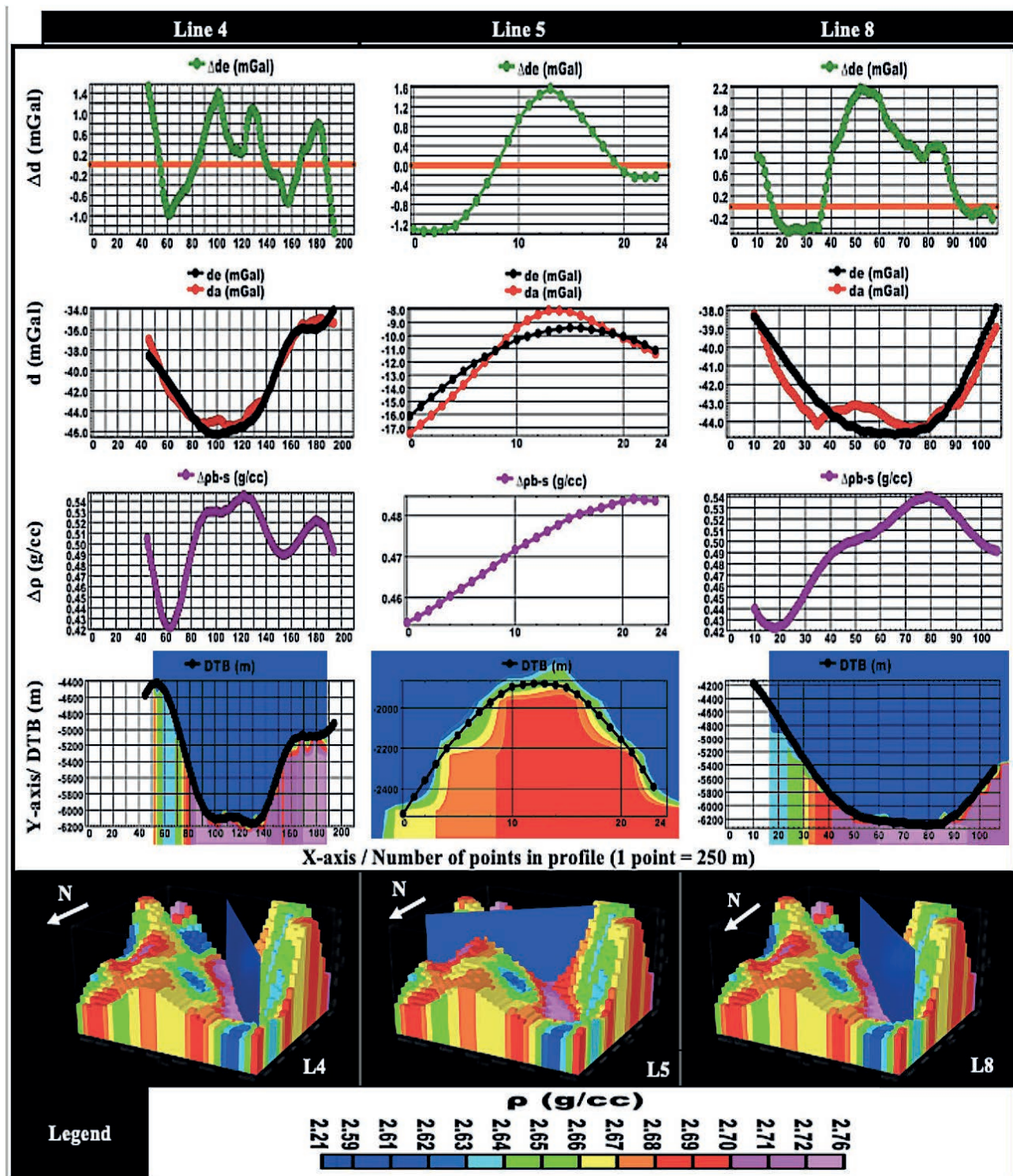


Figure 10.3. An extension of the preceding figures 10.1, 10.2, and 10.3, together illustrating the efficacy of the inversion scheme's third-last stage in extracting two-dimensional gravity models at various seismic line locations (shown in figures 10.1, 10.2, 10.3, and 10.4) for tackling seismic challenges in the research area. The solutions were tested to see if they could optimally identify, with minimal misfit between observed and estimated Bouguer responses, the interface between the basement and the sediment in terms of density contrast and the basement's depth and lateral density distribution. These tests are carried out to better assess the efficiency of the certified 3D extraction source

Рисунок 10.3. Расширение предыдущих рис. 10.1, 10.2 и 10.3, иллюстрирующее эффективность третьего и последнего этапа схемы инверсии при извлечении двумерных гравитационных моделей в различных местоположениях сейсмических линий (показано на рис. 10.1, 10.2, 10.3 и 10.4) для решения сейсмических задач в районе исследований. Решения были протестированы, чтобы увидеть, могут ли они оптимально идентифицировать, с минимальным несоответствием между наблюдаемыми и оцененными откликами Буге, границу раздела между фундаментом и отложениями с точки зрения контраста плотности, а также глубины фундамента и распределения плотности по латерали. Эти испытания проводятся для лучшей оценки эффективности сертифицированного 3D-источника извлечения

3. We examined lateral basement density and basement-sedimentary density contrast in the fourth control test to assess our inversion scheme's inverse density estimations. This control test determined whether a lateral density model could optimize the basement-sedimentary density contrast and determine the basement depth with minimal depth estimate error. Graphs B1, B2, B3, B4, B5, and B6 in fig. 9.1 show the results of this test.

4. This study compared the calculated and actual Bouguer anomalies at nineteen easily accessible control wells. A tertiary control test performed across the region may provide a mean data misfit near zero by terminating the inversion process at regional null offsets. This scenario shows a minimal data misfit consistent with the best solution of the depth-density model. Fig. 9.1, graphs C1, C2, C3, and C4, provide proof of this.

Fig. 9.2, graphs (A2 and A4) demonstrate that the mean basement depth model's sixth optimal inverse trial produced the lowest model calculation error for the first stage of our inversion scheme. First-stage optimality shows a correlation between the actual and estimated basement depths of the six constraint wells in the following order: W8 – 333.6, W13 – 87.8, W15 2.0, W17 138.8, W18 221.2, and W19 55.7 m, as a result of depth estimates in the following sequence: (W8 – 2910.6, W13 – 1216.68, W15 – 3767, W17 – 2023.1, W18 – 2686.7, and W19 – 3995.3 m). In the third stage of our scheme, we adjusted the basement depth model by minimizing the misfit with the best correlation to actual depths using an estimated depth sequence (W8 – 2624, W13 – 1044.2, W15 – 3738.7, W17 – 2135.4, W18 – 2938.3, and W19 – 4035.5 m) with a more significant reduction of the depth misfit sequence (W8 – 46.9, W13 84.7, W15 30.2, W17 26.5, W18 – 30.2, W19 15.4 m). The depth misfit sequence shows that the optimal depth model in the third stage of our scheme is more accurate.

Graph A6 Sequenced percentage depth misfit estimates: In the sixth optimal depth misfit trial, for the first stage, W8 12.9, W13 7.7, W15 – 0.05, W17 – 6.4, W18 – 7.60, and W19 – 1.37 %; for the third stage, W8 1.8, W13 7.5, W15 0.8, W17 1.2, W18 1.0, and W19 – 0.4%.

Graph A8 shows the re-estimated optimal depth misfit sequences relative to the six constraint wells' actual mean basement depth, showing the percentage coefficients of variation for each well. For example, the sixth optimal depth misfit sequence in the first stage is re-estimated by W8 12.0, W13 13.2, W15 – 0.07, W17 – 5.0, W18 – 7.9, and W19 – 2.0%, while in the third stage, W8 1.7, W13 – 3.0, W15 – 1.1, W17 – 0.9, W18 1.1, and W19 – 0.5%.

As illustrated in graphs B3 and B4, the constrained mean density trial was distributed among the six controlled wells by lateral density sequence: W8 2.617, W13 2.668, W15 2.634, W17 2.689, W18 2.665, and W19 2.661 g/cc.

Fig. 9.1. Graph C4 depicts the six wells (W8 – 1.254, W13 – 0.856, W15 – 4.414, W17 1.000, W18 – 0.704, and W19 0.088 mGal) in this data-misfit sequence between estimated and observed data constraints, used to constrain basement depth.

Through extraction of 2D gravity models at seismic lines' locations

5. Our inversion scheme's 3D gravity inverse optimal depth-density model solution's fifth quality control test gen-

erated 2D gravity model cross sections at 2D seismic line locations along the El Zeit basin's underlying basement relief. Fig. 10.1, 10.2, and 10.3 show minimal Bouguer misfits for the 2D optimal solutions of the basement complex lateral density distribution, the basement-sedimentary density contrast interface, and the basement depth.

As shown in fig. 10.1 map A, indicator lines A-A'; B-B'; C-C', and D-D' (width 14056, 14977, and 19066 m * length 25805 m) indicate the asymmetrical basin's width along the northwest-southeast axis, estimated for the southern, middle, and northern parts of the basin. Delineating the optimal basement relief, which depicts the basement-sedimentary density contrast interface, shows this optimal sedimentary basin depth model.

Fig. 10.1B, 10.2, and 10.3 show two-dimensional gravity inversion results along the research area's six seismic lines. Our research area's optimal three-dimensional gravity model was the sixth inverse model trial in the inverse parameterization sequence for the third final stage of our inversion scheme, from which the optimal two-dimensional gravity models were inversely modeled. The approximately minimal calculated inverse data misfit error from this sixth optimal trial validates the 2D extracted model's optimal key parameter values.

Conclusions

The present study employs the GM-SYS-3D inversion code to conduct a multi-dimensional three-stage gravity inversion within the Gebel Zeit area of the southwestern Gulf of Suez. Three strategies are utilized to parameterize the forward modeling process by providing initial approximations and optimizing inverse modeling estimates through multiple iterations. The depth-to-basement, lateral density distribution of the basement complex, and lateral density contrast at the basement-sedimentary interface were estimated using the 3D depth-density model.

A total of six stratigraphic wells, which were accessible with total depths to the basement, were utilized as control measures. The estimated depths to the basement for these basement control wells exhibited an overall 1.63% coefficient of variance in correspondence with their actual total depths to the basement. The discrepancies in depth ranged from – 1.24% to 8% relative to the measured mean depth of the basement and from – 1.24% to 3.8% relative to the total measured depth of each well's basement.

The quantitative analysis of the optimal inverse-recovered model in the third stage exhibited the best-possible correlation with geological data, with a minimal error of 1.63%. The inversion procedure was employed effectively to model the forward behavior of three depth-density scenarios inversely. This model successfully estimated the mean depth of the basement in the study area, which spanned from 0 to 6453 m beyond sea level. The resulting mean Bouguer anomaly misfit was found to be 0.0045 mGal. The average density contrast at the interface between the basement and sedimentary layers is 0.4606 g/cc, exhibiting a lateral variation ranging from 0.5458 to 0.3835. The interface delineates the central basin of the research area.

The presence of salt diapirs challenges basement delineation through seismic interpretation in two dimensions. The inverse problem of accurately recovering the optimal 3D depth-density model was handled through this model's solutions' evaluation at nine seismic lines, resulting in a well-char-

acterized representation of the basement relief. The complete recovery of the residual Bouguer image depicts the effect of the high tectonics of the underlying basement relief on its overlaid thick sedimentary structure in the study area, yielding valuable deep geological insights into the advancement of petroleum resources. The results of this study revealed the presence of a graben system characterized by two prominent normal faults that intersect sedimentary strata, originating from a depth of 6500 meters within the Earth's crust and extending up to the surface. The Gebel Zeit and Esh-Mellaha ranges exhibit geological faults that result in the exposure of underlying basement rocks. The phenomenon of basement shallowing in this particular study area is of significant interest from both tectonic and hydrocarbon perspectives.

The 3D optimal inverse recovery suggests that the study area is characterized by three distinct basement blocks, which have been accurately estimated in terms of depth, density, and density contrast with the overlaid sedimentary blocks. The first block is a downthrown block located in the middle of the area and is covered by a substantial cover of sedimentary deposits. This block is responsible for forming a basin structure known as the El Zeit basin, which reaches a maximum depth of 6453 m. The other two blocks are located on the western and eastern flanks and are considered upthrown blocks. These blocks have zero depths and are associated with the roots of the Gebel Zeit and Esh-Mellaha ranges, respectively. Numerous fault traps can be generated along fault planes where minor half-grabens are formed due to the fault compression within sedimentary layers. This compression leads to the development of elongat-

ed sub-basins above the basement complex. These sub-basins are adjacent to the basement complex, as the basement blocks uplift through the sedimentary layers and are separated from it by small anticlinal structures. These anticlinal structures increase the possibility for fault entrapment in the presence of an overlaid impermeable sedimentary layer above them. The tectonic characteristics of these sedimentary sub-basin structures are attributed to the vertical displacement of the underlying basement blocks, resulting in significant upward pressure and converging towards the central basinal region. The elementary basinal structure in El Zeit experienced tectonic activity, which played a significant role in shaping the Nubia sandstone and creating a deep reservoir formation with a substantial volume of hydrocarbons in the study area. The deep sedimentary column in the middle basinal area has the potential to serve as a source for migrating hydrocarbons through the fault planes where low pressures exist. This migration is best possibly entrapment along the hanging wall sedimentary block above the eastern and western fault planes, where small anticlinal structures can form between the compressed sedimentary structures and the fault planes. The basement foot wall block on the other sides of the fault planes laterally seals these anticlinal structures. The impermeable sedimentary layers' formations may also vertically seal them.

Disclosure of Funding Sources

The researcher Ahmed G. M. Hassan is funded by a scholarship [EGY-6958/16] under the joint (executive program between Arab republic of Egypt and Russia).

REFERENCES

1. Jessell M. et al. 2014, Next Generation Three-Dimensional Geologic Modeling and Inversion. Building Exploration Capability for the 21st Century. Chapter 13. Karen D. Kelley and Howard C. Golden (eds). Littleton, Colorado, USA: Society of Economic Geologists, , pp. 261–272. <https://doi.org/10.5382/SP.18.13>
2. Fan D., Li S., Li X., Yang J., Wan X. 2021, Seafloor Topography Estimation from Gravity Anomaly and Vertical Gravity Gradient Using Nonlinear Iterative Least Square Method. *Remote Sensing*, vol. 13, pp. 1–19. <https://doi.org/10.3390/rs13010064>
3. Silva J. B. C., Santos D. F., Gomes K. P. 2014, Fast gravity inversion of basement relief. *Geophysics*, vol. 79, no. 5, pp. G79–G91. <https://doi.org/10.1190/geo2014-0024.1>
4. Pham L. T., Oksum E., Do T. D. 2018, GCH_gravinv: A MATLAB-based program for inverting gravity anomalies over sedimentary basins. *Computers & Geosciences*, vol. 120, pp. 40–47. <https://doi.org/10.1016/j.cageo.2018.07.009>
5. Cremon M., Burnham A. K., Liu Y., Lapene A. 2017, Modified Athy-Law Compaction to Account for Porosity Generation and Preservation from Kerogen Conversion in Terzaghi-Like Models of Petroleum Source Rocks. AAPG Annual Convention and Exhibition, article number 42062, pp. 1–18.
6. Wu L. 2018, Efficient Modeling of Gravity Fields Caused by Sources with Arbitrary Geometry and Arbitrary Density Distribution. *Surveys in Geophysics*, vol. 39, issue 3, pp. 401–434. <https://doi.org/10.1007/s10712-018-9461-7>
7. Santos D. F., Silva J. B. C., Martins C. M., Santos R. C. S., Ramos L. C., de Araújo A. C. M. 2015, Efficient gravity inversion of discontinuous basement relief. *Geophysics*, vol. 80, no. 4, pp. G95–G106. <https://doi.org/10.1190/geo2014-0513.1>
8. Preston L., Poppeliers C., Schodt D. J. 2020, Seismic Characterization of the Nevada National Security Site Using Joint Body Wave, Surface Wave, and Gravity Inversion. *Bulletin of the Seismological Society of America*, vol. 110, no. 1, pp. 110–126. <http://dx.doi.org/10.1785/0120190151>
9. Wu L. 2019, Fourier-domain modeling of gravity effects caused by polyhedral bodies. *Journal of Geodesy*, vol. 93, issue 5, pp. 635–653. <http://dx.doi.org/10.1007/s00190-018-1187-2>
10. Mallesh K., Chakravarthi V., Ramamma B. 2019, 3D Gravity Analysis in the Spatial Domain: Model Simulation by Multiple Polygonal Cross-Sections Coupled with Exponential Density Contrast. *Pure and Applied Geophysics*, vol. 176, issue 6, pp. 2497–2511. <https://doi.org/10.1007/s00024-019-02103-9>
11. Wu L. 2016, Efficient modelling of gravity effects due to topographic masses using the Gauss–FFT method. *Geophysical Journal International*, vol. 205, issue 1, pp. 160–178. <https://doi.org/10.1093/gji/ggw010>
12. Wu L., Lin Q. 2017, Improved Parker's method for topographic models using Chebyshev series and low rank approximation. *Geophysical Journal International*, vol. 209, issue 2, pp. 1296–1325. <https://doi.org/10.1093/gji/ggx093>
13. Stolk W., Kaban M., Beekman F., Tesauro M., Mooney W. D., Cloetingh S. 2013, High resolution regional crustal models from irregularly distributed data: Application to Asia and adjacent areas. *Tectonophysics*, vol. 602, no. 6, pp. 55–68. <https://doi.org/10.1016/j.tecto.2013.01.022>
14. Buccini A. 2016, Tikhonov-type iterative regularization methods for ill-posed inverse problems: theoretical aspects and applications: PhD thesis. Varese, Italy: Università degli Studi dell'Insubria.
15. Dadak B. 2017, Inversion of gravity data for depth-to-basement estimate using the volume and surface integral methods: model and case study. Salt Lake City, UT, USA: The University of Utah, May, 92 p.
16. Maag E., Li Y. 2018, Discrete-valued gravity inversion using the guided fuzzy c-means clustering technique. *Geophysics*, vol. 83, issue 4, pp. 1–115. <http://dx.doi.org/10.1190/geo2017-0594.1>

17. Feng X., Wang W., Yuan B. 2018, 3D gravity inversion of basement relief for a rift basin based on combined multinorm and normalized vertical derivative of the total horizontal derivative techniques. *Geophysics*, vol. 83, issue 5, pp. G107–G118. <https://doi.org/10.1190/geo2017-0678.1>
18. Celli F., Nappi R., Paoletti V., Florio G. 2021, Basement Mapping of the Fucino Basin in Central Italy by ITRESC Modeling of Gravity Data. *Geosciences*, vol. 11, no. 10, pp. 1–25. <https://doi.org/10.3390/geosciences11100398>
19. Ren Z., Chen C., Pan K., Kalscheuer T., Maurer H., Tang J. 2017, Gravity Anomalies of Arbitrary 3D Polyhedral Bodies with Horizontal and Vertical Mass Contrasts. *Surveys in Geophysics*, vol. 38, no. 2, pp. 479–502. <https://doi.org/10.1007/s10712-016-9395-x>
20. Vatankhah S., Renaud R. A., Huang X., Mickus K., Gharloghi M. 2022, Large-scale focusing joint inversion of gravity and magnetic data with Gramian constraint. *Geophysical Journal International*, vol. 230, issue 3, pp. 1585–1611. <https://doi.org/10.1093/gji/ggac138>
21. Makled W. A., Ashwah A. A. E., Lotfy M. M., Hegazey R. M. 2020, Anatomy of the organic carbon related to the Miocene syn-rift dysoxia of the Rudeis Formation based on foraminiferal indicators and palynofacies analysis in the Gulf of Suez, Egypt. *Marine and Petroleum Geology*, vol. 111, pp. 695–719. <https://doi.org/10.1016/j.marpetgeo.2019.08.048>
22. Abuzied S. M., Kaiser M. F., Shendi E.-A. H., Abdel-Fattah M. I. 2020, Multi-criteria decision support for geothermal resources exploration based on remote sensing, GIS and geophysical techniques along the Gulf of Suez coastal area, Egypt. *Geothermics*, vol. 88, article number 101893. <https://doi.org/10.1016/j.geothermics.2020.101893>
23. 2019, The Geology of the Arab World – An Overview. Bendaoud A., Hamimi Z., Hamoudi M., Djemai S., Zoheir B. (eds). Berlin: Springer, 560 p.
24. Temraz M., Dypvik H. 2018, The Lower Miocene Nukhul Formation (Gulf of Suez, Egypt): microfacies and reservoir characteristics. *Journal of Petroleum Exploration and Production Technology*, vol. 8, no. 1, pp. 85–98. <https://doi.org/10.1007/s13202-017-0386-3>
25. Van Dijk J., AlBloushi A., Ajayi A. T., De Vincenzi L., Ellen H., Guney H., Holloway P., Khdaouria M., Mcleod I. S. 2019, Hydrocarbon exploration and production potential of the Gulf of Suez Basin in the framework of the new tectonostratigraphic model. SPE Gas & Oil Technology Showcase and Conference (October 21–23, 2019 Dubai, UAE). Article number SPE-198622-MS. <https://doi.org/10.2118/198622-MS>
26. Farouk S., Sen S., Pigott J. D., Sarhan M. A. 2022, Reservoir characterization of the middle Miocene Kareem sandstones, Southern Gulf of Suez Basin, Egypt. *Geomechanics and Geophysics for Geo-Energy and Geo-Resources*, vol. 8, no. 5, pp. 1–17. <https://doi.org/10.1007/s40948-022-00437-8>
27. Embabi A. M., Abdelwahhab M. A., Abdelhafez N. A. 2021, Reservoir characterization and petroleum geology at esh el Mallaha field, southern Gulf of Suez, Egypt. *Al-Azhar Bulletin of Science*, vol. 32, no. 2, pp. 1–12. <https://doi.org/10.21608/absb.2021.89127.1130>
28. Hadad Y. T., Hakimi M. H., Abdullah W. H., Kinawy M., El Mahdy O., Lashin A. 2021, Organic geochemical characteristics of Zeit source rock from Red Sea Basin and their contribution to organic matter enrichment and hydrocarbon generation potential. *Journal of African Earth Sciences*, vol. 177, article number 104151. <https://doi.org/10.1016/j.jafrearsci.2021.104151>
29. 2017, The geology of Egypt: Regional Geology Reviews. R. Said (ed.), 734 p. <https://doi.org/10.1201/9780203736678>
30. Almaliki K. A., Mahmud S. A. 2018, Gulfs of Suez and Aqaba: New insights from recent satellite-marine potential field data. *Journal of African Earth Sciences*, vol. 137, pp. 116–132. <https://doi.org/10.1016/j.jafrearsci.2017.10.004>
31. El Gammal R. M. H., Orabi H. 2019, Coniacian-late Campanian Planktonic Events in the Duwi Formation, Red Sea region, Egypt. *Journal of Geology & Geophysics*, vol. 8, issue 1, pp. 1–16. <http://dx.doi.org/10.4172/2381-8719.1000456>
32. Attia I., Helal I., El Dakhakhny A., Aly S. A. 2017, Using sequence stratigraphic approaches in a highly tectonic area: Case study – Nubia (A) sandstone in southwestern Gulf of Suez, Egypt. *Journal of African Earth Sciences*, vol. 136, pp. 10–21. <https://doi.org/10.1016/j.jafrearsci.2017.06.001>
33. Afifi A. S., Moustafa A. R., Helmy H. M. 2016, Fault block rotation and footwall erosion in the southern Suez rift: Implications for hydrocarbon exploration. *Marine and Petroleum Geology*, vol. 76, pp. 377–396. <https://doi.org/10.1016/j.marpetgeo.2016.05.029>
34. Youssef M., El-Sorogy A., El-Sabrouty M., Al-Otaibi H. 2016, Invertebrate shells as pollution bio-indicators, Gebel El-Zeit area, Gulf of Suez, Egypt. *Indian Journal of Geo-Marine Sciences*, vol. 45, no. 5, pp. 687–695.
35. 2016, Ministry of Petroleum and Mineral Resources. Ganoub El-Wadi Petroleum Holding Company “Ganope”. International Bid Round 2016, pp. 1–7.
36. South H. et al. The Source for Critical information and insight. Global Exploration & production service, Gulf of Suez south, Egypt. Status of Carto Data and IRIS21 databases. 2009.
37. Aboud E., Salem A., Ushijima K. 2005, Subsurface structural mapping of Gebel El-Zeit area , Gulf of Suez, Egypt using aeromagnetic data. *Earth, Planets and Space*, vol. 57, pp. 755–760. <http://dx.doi.org/10.1186/BF03351854>

The article was received on August 09, 2023

Многоступенчатая схема 3D-гравитационной инверсии для максимальной оптимизации модели подземного фундамента в бассейне Гебель-Эль-Зейт, юго-западная часть Суэцкого залива, Египет

Ахмед Гамаль Мохамед ХАССАН^{1,2}

Карам Самир Ибрагим ФАРАГ³

Алаа Ахмед Фахми АРЕФ²

Алексей Лазаревич ПИСКАРЕВ¹

¹Санкт-Петербургский государственный университет, Санкт-Петербург, Россия

²Управление по ядерным материалам (УЯМ), Каир, Египет

³Университет Айн-Шамс, Каир, Египет

Аннотация

Актуальность и цель работы. Благодаря блоковой структуре фундамента в осадочном бассейне, юго-западная часть Суэцкого залива в бассейне Гебель-Эль-Зейт является одним из самых привлекательных углеводородных горных отводов Египта. Однако соляные покровы в осадочных слоях затрудняют интерпретацию сейсмических данных в этом районе, что осложняет построение трехмерной первичной структуры центрального бассейна. В этом исследовании гравитационные аномалии Буге используются для ввода предположений модели сложной латеральной плотности фундамента для определения оптимальной трехмерной глубины фундамента для исследуемой территории.

Методология исследования. Основываясь на концепции последовательных подходов к трехмерной спектральной инверсии слоистой среды, посредством испытаний с Ольденбургской и другими прямыми моделями, многие стратегии прямой оптимизации и последовательности параметризации с предположениями о переменных ограничениях использовались для регулирования операций инверсии в рамках предложенной трехэтапной схемы гравитационной инверсии для определения оптимального решения по глубине и плотности с минимальным несоответствием расчетных данных. В этом исследовании статистически анализируется рельеф фундамента и сложное распределение плотности по латерали, чтобы определить наилучшие параметры для создания трехмерной модели глубины и плотности. Нулевые региональное значение силы тяжести и регулярная помеха, которые привели к тому, что средняя ошибка была равна нулю, помогли смо-делировать наилучшие возможные ограничивающие предположения модели боковой плотности.

Результаты и выводы. Корреляционные данные по глубинам многих стратиграфически-контрольных скважин, пробуренных на инверсивной 3D-модели фундамента, подтвердили оптимальность рельефа фундамента изучаемой территории. Корреляционный анализ показал хорошее соответствие между прогнозируемыми и измеренными глубинами, доказав полученную оптимальность латерального распределения плотности фундаментного комплекса, минимизируя ошибку расчета глубины до минимального процента.

Ключевые слова: Египет, Суэцкий залив, район бассейна Эль-Зейт, аномалии Буге, схема спектрально-слоистой гравитационной инверсии, параметризация и оптимизация.

Исследования Ахмеда Г. М. Хасана финансируются за счет стипендии [EGY-6958/16] в рамках совместной (исполнительской) программы между Арабской Республикой Египет и Россией.

REFERENCES

1. Jessell M. et al. Next Generation Three-Dimensional Geologic Modeling and Inversion. Building Exploration Capability for the 21st Century. Chapter 13. Karen D. Kelley and Howard C. Golden (eds). Littleton, Colorado, USA: Society of Economic Geologists, 2014. P. 261–272. <https://doi.org/10.5382/SP.18.13>
2. Fan D., Li S., Li X., Yang J., Wan X. Seafloor Topography Estimation from Gravity Anomaly and Vertical Gravity Gradient Using Nonlinear Iterative Least Square Method // Remote Sensing. 2021. Vol. 13. Pp. 1–19. <https://doi.org/10.3390/rs13010064>
3. Silva J. B. C., Santos D. F., Gomes K. P. Fast gravity inversion of basement relief // Geophysics. 2014. Vol. 79. No. 5. Pp. G79–G91. <https://doi.org/10.1190/geo2014-0024.1>
4. Pham L. T., Oksum E., Do T. D. GCH_gravinv: A MATLAB-based program for inverting gravity anomalies over sedimentary basins // Computers & Geosciences. 2018. Vol. 120. P. 40–47. <https://doi.org/10.1016/j.cageo.2018.07.009>
5. Cremon M., Burnham A. K., Liu Y., Lapene A. Modified Athy-Law Compaction to Account for Porosity Generation and Preservation from Kerogen Conversion in Terzaghi-Like Models of Petroleum Source Rocks // AAPG Annual Convention and Exhibition. 2017. Article number 42062. P. 1–18.

6. Wu L. Efficient Modeling of Gravity Fields Caused by Sources with Arbitrary Geometry and Arbitrary Density Distribution // *Surveys in Geophysics*. 2018. Vol. 39. Issue 3. P. 401–434. <https://doi.org/10.1007/s10712-018-9461-7>
7. Santos D. F., Silva J. B. C., Martins C. M., Santos R. C. S., Ramos L. C., de Araújo A. C. M. Efficient gravity inversion of discontinuous basement relief // *Geophysics*. 2015. Vol. 80. No. 4. P. G95–G106. <https://doi.org/10.1190/geo2014-0513.1>
8. Preston L., Poppeliers C., Schodt D. J. Seismic Characterization of the Nevada National Security Site Using Joint Body Wave, Surface Wave, and Gravity Inversion // *Bulletin of The Seismological Society of America*. 2020. Vol. 110. No. 1. P. 110–126. <http://dx.doi.org/10.1785/0120190151>
9. Wu L. Fourier-domain modeling of gravity effects caused by polyhedral bodies // *Journal Of Geodesy*. 2019. Vol. 93. Issue 5. P. 635–653. <http://dx.doi.org/10.1007/s00190-018-1187-2>
10. Mallesh K., Chakravarthi V., Ramamma B. 3D Gravity Analysis in the Spatial Domain: Model Simulation by Multiple Polygonal Cross-Sections Coupled with Exponential Density Contrast // *Pure And Applied Geophysics*. 2019. Vol. 176. Issue 6. Pp. 2497–2511. <https://doi.org/10.1007/s00024-019-02103-9>
11. Wu L. Efficient modelling of gravity effects due to topographic masses using the Gauss–FFT method // *Geophysical Journal International*. 2016. Vol. 205. Issue 1. P. 160–178. <https://doi.org/10.1093/gji/ggw010>
12. Wu L., Lin Q. Improved Parker's method for topographic models using Chebyshev series and low rank approximation // *Geophysical Journal International*. 2017. Vol. 209. Issue 2. P. 1296–1325. <https://doi.org/10.1093/gji/ggx093>
13. Stolk W., Kaban M., Beekman F., Tesauro M., Mooney W. D., Cloetingh S. 2013, High resolution regional crustal models from irregularly distributed data: Application to Asia and adjacent areas // *Tectonophysics*. Vol. 602. No. 6. P. 55–68. <https://doi.org/10.1016/j.tecto.2013.01.022>
14. Buccini A. Tikhonov-type iterative regularization methods for ill-posed inverse problems: theoretical aspects and applications: PhD thesis. Varese, Italy: Università degli Studi dell'Insubria, 2016.
15. Dadak B. Inversion of gravity data for depth-to-basement estimate using the volume and surface integral methods: model and case study. Salt Lake City, UT, USA: The University of Utah, May, 2017. 92 p.
16. Maag E., Li Y. Discrete-valued gravity inversion using the guided fuzzy c-means clustering technique // *Geophysics*. 2018. Vol. 83. Issue 4. P. 1–115. <http://dx.doi.org/10.1190/geo2017-0594.1>
17. Feng X., Wang W., Yuan B. 3D gravity inversion of basement relief for a rift basin based on combined multinorm and normalized vertical derivative of the total horizontal derivative techniques // *Geophysics*. 2018. Vol. 83. Issue 5. P. G107–G118. <https://doi.org/10.1190/geo2017-0678.1>
18. Cella F., Nappi R., Paoletti V., Florio G. Basement Mapping of the Fucino Basin in Central Italy by ITRESC Modeling of Gravity Data // *Geosciences*. 2021. Vol. 11. No. 10. P. 1–25. <https://doi.org/10.3390/geosciences11100398>
19. Ren Z., Chen C., Pan K., Kalscheuer T., Maurer H., Tang J. Gravity Anomalies of Arbitrary 3D Polyhedral Bodies with Horizontal and Vertical Mass Contrasts // *Surveys In Geophysics*. 2017. Vol. 38. No. 2. P. 479–502. <https://doi.org/10.1007/s10712-016-9395-x>
20. Vatankhah S., Renaud R. A., Huang X., Mickus K., Gharloghi M. Large-scale focusing joint inversion of gravity and magnetic data with Gramian constraint // *Geophysical Journal International*. 2022. Vol. 230. Issue 3. P. 1585–1611. <https://doi.org/10.1093/gji/ggac138>
21. Makled W. A., Ashwah A. A. E. E., Lotfy M. M., Hegazey R. M. Anatomy of the organic carbon related to the Miocene syn-rift dysoxia of the Rudeis Formation based on foraminiferal indicators and palynofacies analysis in the Gulf of Suez, Egypt // *Marine and Petroleum Geology*. 2020. Vol. 111. P. 695–719. <https://doi.org/10.1016/j.marpetgeo.2019.08.048>
22. Abuzied S. M., Kaiser M. F., Shendi E.-A. H., Abdel-Fattah M. I. Multi-criteria decision support for geothermal resources exploration based on remote sensing, GIS and geophysical techniques along the Gulf of Suez coastal area, Egypt // *Geothermics*. 2020. Vol. 88. Article number 101893. <https://doi.org/10.1016/j.geothermics.2020.101893>
23. The Geology of the Arab World – An Overview. Bendaoud A., Hamimi Z., Hamoudi M., Djemai S., Zoheir B. (eds). Berlin: Springer, 2019. 560 p.
24. Temraz M., Dypvik H. The Lower Miocene Nukhul Formation (Gulf of Suez, Egypt): microfacies and reservoir characteristics // *Journal of Petroleum Exploration and Production Technology*. 2018. Vol. 8. No. 1. P. 85–98. <https://doi.org/10.1007/s13202-017-0386-3>
25. Van Dijk J., AlBloushi A., Ajayi A. T., De Vincenzi L., Ellen H., Guney H., Holloway P., Khdaouria M., Mcleod I. S. Hydrocarbon exploration and production potential of the Gulf of Suez Basin in the framework of the new tectonostratigraphic model. SPE Gas & Oil Technology Showcase and Conference (October 21–23, 2019 Dubai, UAE). 2019. Article number SPE-198622-MS. <https://doi.org/10.2118/198622-MS>
26. Farouk S., Sen S., Pigott J. D., Sarhan M. A. Reservoir characterization of the middle Miocene Kareem sandstones, Southern Gulf of Suez Basin, Egypt // *Geomechanics and Geophysics for Geo-Energy and Geo-Resources*. 2022. Vol. 8. No. 5. P. 1–17. <https://doi.org/10.1007/s40948-022-00437-8>
27. Embabi A. M., Abdelwahhab M. A., Abdelhafez N. A. Reservoir characterization and petroleum geology at esh el Mallaha field, southern Gulf of Suez, Egypt // *Al-Azhar Bulletin of Science*. 2021. Vol. 32. No. 2. P. 1–12. <https://doi.org/10.21608/absb.2021.89127.1130>
28. Hadad Y. T., Hakimi M. H., Abdullah W. H., Kinawy M., El Mahdy O., Lashin A. Organic geochemical characteristics of Zeit source rock from Red Sea Basin and their contribution to organic matter enrichment and hydrocarbon generation potential // *Journal of African Earth Sciences*. 2021. Vol. 177. Article number 104151. <https://doi.org/10.1016/j.jafrearsci.2021.104151>
29. The geology of Egypt: Regional Geology Reviews. R. Said (ed.), 2017. 734 p. <https://doi.org/10.1201/9780203736678>
30. Almalki K. A., Mahmud S. A. Gulfs of Suez and Aqaba: New insights from recent satellite-marine potential field data // *Journal of African Earth Sciences*. 2018. Vol. 137. P. 116–132. <https://doi.org/10.1016/j.jafrearsci.2017.10.004>
31. El Gammal R. M. H., Orabi H. Coniacian-late Campanian Planktonic Events in the Duwi Formation, Red Sea region, Egypt // *Journal of Geology & Geophysics*. 2019. Vol. 8. Issue 1. P. 1–16. <http://dx.doi.org/10.4172/2381-8719.1000456>
32. Attia I., Helal I., El Dakhakhny A., Aly S. A. Using sequence stratigraphic approaches in a highly tectonic area: Case study – Nubia (A) sandstone in southwestern Gulf of Suez, Egypt // *Journal of African Earth Sciences*. 2017. Vol. 136. P. 10–21. <https://doi.org/10.1016/j.jafrearsci.2017.06.001>
33. Afifi A. S., Moustafa A. R., Helmy H. M. Fault block rotation and footwall erosion in the southern Suez rift: Implications for hydrocarbon exploration // *Marine and Petroleum Geology*. 2016. Vol. 76. P. 377–396. <https://doi.org/10.1016/j.marpetgeo.2016.05.029>
34. Youssef M., El-Sorogy A., El-Sabrouty M., Al-Otaibi H. Invertebrate shells as pollution bio-indicators, Gebel El-Zeit area, Gulf of Suez, Egypt // *Indian Journal of Geo-Marine Sciences*. 2016. Vol. 45. No. 5. P. 687–695.
35. Ministry of Petroleum and Mineral Resources. Ganoub El-Wadi Petroleum Holding Company "Ganope". International Bid Round 2016. 2016. P. 1–7.
36. South H. et al. The Source for Critical information and insight. Global Exploration & production service, Gulf of Suez south, Egypt. Status of Carto Data and IRIS21 databases. 2009.
37. Aboud E., Salem A., Ushijima K. Subsurface structural mapping of Gebel El-Zeit area , Gulf of Suez, Egypt using aeromagnetic data // *Earth, Planets and Space*. 2005. Vol. 57. P. 755–760. <http://dx.doi.org/10.1186/BF03351854>

Статья поступила в редакцию 09 августа 2023 года